Deep-Sea Research II, Palmer LTER Special Issue

On the characteristics of internal tides and coastal upwelling behaviour in Marguerite Bay, west Antarctic Peninsula

Margaret I. Wallace[1,2*], Michael P. Meredith[2], Mark A. Brandon[1], Toby J. Sherwin[3], Andrew Dale[3], Andrew Clarke[2]

[1] Centre for Earth, Planetary, Space and Astronomical Research, The Open University, Walton Hall, Milton Keynes, U.K, MK6 7AA.

[2] British Antarctic Survey, High Cross, Madingley Road, Cambridge, U.K, CB3 0ET.

[3] The Scottish Association for Marine Science, Dunstaffnage Marine Laboratory, Oban, Argyll, U.K, PA37 1QA.

Margaret Wallace (corresponding author): m.i.wallace@open.ac.uk

Tel: +44 (0)1223 221260

Fax: +44 (0)1223 221226

Michael Meredith: mmm@bas.ac.uk

Mark Brandon: m.a.brandon@open.ac.uk

Toby Sherwin: Toby.Sherwin@sams.ac.uk

Andrew Dale: Andrew.Dale@sams.ac.uk

Andrew Clarke: accl@bas.ac.uk

Abstract

Internal waves and coastal upwelling have important roles in both physical oceanography and marine ecosystems, via processes such as mixing of water masses and transfer of heat and nutrients to biologically active layers. In this paper we use quasi-weekly hydrographic profiles and moored records of temperature, salinity and water velocity to investigate the nature of internal tides and coastal upwelling behaviour in northern Marguerite Bay at the western Antarctic Peninsula. Within Ryder Bay, a near-coastal site in northern Marguerite Bay, atmospherically-forced oscillations of the water column with periods around 2-7 days are observed, associated with wind-induced coastal upwelling and downwelling. Sea ice cover is seen to play a role in the seasonal suppression of these oscillations. Significant internal tides are also observed at this site. A range of processes are seen to be important in controlling internal tide variability, including changes in local stratification and sea ice conditions. Both diurnal and semi-diurnal internal tidal species are observed, despite the study region being poleward of the critical latitude for diurnal internal tides. This suggests that at least the diurnal internal tides are generated close to the study location, and we investigate likely sources. Our work adds understanding to how such phenomena are generated, and what controls their variability, in a region of rapid physical change and profound ecosystem importance.

Keywords: Coastal upwelling, Internal tides, Sea ice, Antarctic Peninsula, Marguerite Bay

1. Introduction

Both ocean upwelling and internal gravity waves are key phenomena in physical oceanography and have an impact upon marine ecology. Coastal upwelling and downwelling arise predominantly as a result of alongshore wind stress and the divergence of Ekman transport at the coast (Mitchum & Clarke, 1986), such that the tilt in the upwelled density structure is balanced by alongshore geostrophic flow. Coastal upwelling is predominantly an advective process that can lead to increased biological productivity, as the deep, upwelled waters are often nutrient-rich compared with those at the surface (e.g. Halpern, 1976; Winant, 1980; Small & Menzies, 1981). Conversely, downwelling has the potential to move biomass out of the light-favourable, shallow water environment, whilst both mechanisms can disrupt stable stratification via processes such as convection and mixing, leading to low gradients in properties such as density, temperature, salinity and chlorophyll.

Internal waves can also lead to mixing, particularly where interaction of the wave with topography leads to reflection and breaking, and potential redistribution of heat, salt and nutrients. There has been significant work on the barotropic-to-baroclinic tidal energy transfer at fjord sills (see Stigebrandt, 1999, for a review), and numerous studies have concluded that the vertical mixing and circulation in fjords is predominantly driven by such processes (e.g. Stigebrandt, 1976; Stigebrandt & Aure, 1989; Simpson & Rippeth, 1993). The interaction between internal waves and the seabed may induce wave breaking, the formation of local regions of high shear, and enhanced turbulence; these lead to dissipation of the internal wave energy (e.g. Polzin et al., 1997). Similar processes have been observed on the continental shelf (New,

1988; Sherwin, 1988; New & Pingree, 1990; Rippeth & Inall, 2002), whilst diapycnal mixing in the deep ocean away from topography is also driven predominantly by internal wave activity (Munk & Wunsch, 1998). Internal tides have been observed in both the Arctic (Konyaev et al., 2000; Konyaev, 2000; Morozov et al., 2003) and the ocean close to Antarctica (Foldvik et al., 1990; Levine et al., 1997; Albrecht et al., 2006), and modelling work has suggested that these features are locally generated via the interaction of barotropic tides with seabed topography (e.g. Morozov & Pisarev, 2002; Padman et al., 2006). However, the role of internal tides in mixing is not well constrained, and studies have shown that tidally-induced mixing can be small, even in the presence of energetic baroclinic tides (e.g. Muench et al., 2002; Padman et al., 2006).

Internal waves can arise from a number of sources, including the interaction of currents, such as barotropic tides and wind-induced flows, with seabed topography (e.g. New, 1988; Stigebrandt, 1999; Levine et al., 1997). Once generated, linear wave theory predicts that freely propagating waves are restricted to a frequency, ω, where $f^2<\omega^2$, and f is the inertial frequency (LeBlond & Mysak, 1978). Thus, for any wave with a period greater than 12 hours, there is a critical latitude beyond which it cannot propagate freely because its frequency is less than f. In reality, seabed topography disrupts this simple theory (LeBlond & Mysak, 1978), and internal waves can be generated poleward of the critical latitude and propagate along a bathymetric barrier (such as the coastline or a sloping bottom), confined to within approximately one internal Rossby radius of the barrier (Emery & Thomson, 2004). The critical latitude for a diurnal internal tide is ~30˚ in both hemispheres, whilst those for the M2 and S2 semidiurnal internal tides are ~75˚ and ~85˚, respectively, placing all polar oceans

beyond the critical latitude for diurnal internal tides and some beyond those for semidiurnal internal tides. Here, we investigate observations of both internal tides and atmospherically forced coastal upwelling/downwelling in Marguerite Bay, west Antarctic Peninsula, between January 2005 and April 2007.

2. Western Antarctic Peninsula shelf waters

The western Antarctic Peninsula (WAP) shelf (Figure 1) **[insert Figure 1 here]** is deep compared with most of the world's shelf seas (much of the shelf is >500m deep), and features rough bathymetry and numerous deep troughs (≤ 1600m) carved by glacial scouring. Offshore of the WAP shelf slope lies the southern boundary of the Antarctic Circumpolar Current (ACC; e.g. Hofmann & Klinck, 1998; Klinck, 1998), which brings warm, saline Circumpolar Deep Water (CDW) close to the slope, from where it can access the shelf (e.g. Martinson et al., this issue). The glacial troughs are preferential routes for this intrusion of CDW, and the less-dense variety of this water mass (Upper CDW; UCDW) in particular accesses the shelf via this route (Klinck et al., 2004). Above UCDW lies the seasonally-varying Antarctic Surface Water (AASW), which is separated from the underlying waters by a permanent pycnocline at ~150-200m (Beardsley et al., 2004; Hofmann & Klinck, 1998; Smith et al., 1999). The depth of this boundary is linked to sea ice conditions, with a generally deeper pycnocline in years with sea ice production greater than the temporal mean (Smith & Klinck, 2002; Meredith et al., 2004). Vertical transfer of heat across the pycnocline from the UCDW to AASW leads to relatively low rates of sea ice production in the area, ensuring that surface waters under present climate conditions do not become denser than the underlying modified UCDW and thereby prohibiting the formation of

126 dense deep and bottom waters (Martinson et al., this issue). During winter, pack ice
127 covers the shelf and the surface layer is uniformly mixed to 100m depth or more, with
128 water at or near the freezing point (temperature, *T*, ~ -1.8˚C) (Smith et al., 1999;
129 Meredith et al., 2004). Salinity is increased via brine rejection during ice production,
130 resulting in mixed-layer salinity, *S*, of approximately 34.1 during winter (Toole, 1981;
131 Klinck et al., 2004). In summer, shallow surface layers (20-30m) are freshened by ice
132 melt and warmed by solar heating; these overlie the remnant of the winter mixed
133 layer, which is now termed Winter Water (WW). This persists during summer as a
134 relative vertical minimum in temperature at ~70-100m (Klinck, 1998; Klinck et al.,
135 2004), though occasionally as deep as 150m (Meredith et al, 2004). Over summer and
136 autumn, increased storm activity leads to the breakdown of these layers and remnant
137 WW undergoes mixing with surface and subpycnocline waters, leading to erosion of
138 the WW signature in areas such as Ryder Bay (Meredith et al., 2004). This does not
139 appear to be a shelf-wide process, however, as data from west of Adelaide Island
140 show the presence of the typical WW minimum well into autumn (e.g. Klinck et al.,
141 2004).
142
143 On the WAP shelf, UCDW intrusions mix with AASW to produce modified UCDW,
144 which has properties intermediate between the two water masses, and are thus crucial
145 for the heat and salt budgets of the region (Hofmann & Klinck, 1998; Klinck, 1998;
146 Smith et al., 1999; Smith & Klinck, 2002; Martinson et al., this issue). Several studies
147 suggest that internal wave activity and localised mixing over the rugged topography
148 may play a role in this process (Klinck, 1998; Smith & Klinck, 2002; Dinniman &
149 Klinck, 2004), whilst Howard et al. (2004) concluded that coastal upwelling could be
150 a significant factor contributing to the upward flux of UCDW properties and has the

potential to raise UCDW into the depth range affected directly by surface stress. The role of these processes in mixing is the subject of ongoing investigations.

Due to its high primary productivity, the WAP continental shelf supports a large biomass of Antarctic krill (Ross et al., 1996a), and consequently large populations of higher predators such as penguins (Fraser & Trivelpiece, 1996) and seals (Costa & Crocker, 1996). This biological productivity is strongly linked to physical processes (Ross et al., 1996b), so internal wave- or upwelling-induced disruption of stratification, both of which influence nutrient and phytoplankton distribution (e.g. Small & Menzies, 1981; Ostrovsky et al., 1996; Mackinnon & Gregg, 2005), have the potential to affect the entire marine ecosystem of the region. Such mixing is also known to influence the redistribution of heat in the upper ocean (e.g. Gregg, 1987; Mackinnon & Gregg, 2005; Winant, 1980), which has the potential to influence sea ice conditions, whilst tidally-forced currents are known to influence sea ice conditions via processes such as lead formation (e.g. Kowalik & Proshutinsky, 1994; Wadhams, 2000; Koentopp et al., 2005). Therefore, both coastal upwelling/downwelling and internal wave activity can be expected to have a significant impact upon a seasonally sea ice-covered region of high biological productivity such as Marguerite Bay. In this paper we investigate these phenomena, using a combination of observational data and theoretical considerations.

3. Methods

To investigate internal wave and coastal upwelling activity in northern Marguerite Bay we use two data sources. The first is part of the British Antarctic Survey's

Rothera Biological and Oceanographic Time Series Study (RaTS; Clarke et al., this issue). As part of RaTS, a year-round time series of conductivity-temperature-depth (CTD) profiles from a nearshore location in Ryder Bay (a small embayment at the northern end of Marguerite Bay; 67˚34.20'S, 68˚13.50'W; 520m water depth; Figure 1) has been collected since 1998. These data have been supplemented in recent years by our second source of data: fixed moorings at both the RaTS site (location above) and an offshore location in a deep glacial trough on the WAP continental shelf (67° 55.39'S, 68° 24.15'W; 840m water depth; Figure 1). This trough lies off the main axis of Marguerite Trough and the mooring is hereafter referred to as MT. In this paper, we focus on data from the quasi-weekly RaTS CTD casts in conjunction with moored CTD, temperature-depth recorder (TDR), temperature recorder (TR) and Acoustic Doppler Current Profiler (ADCP) time series from both moorings.

Moored data are summarized in Table 1 **[insert Table 1 here]** and were collected from the RaTS site for January 2005 – April 2007 (three consecutive deployments) over the depth range ~0-280m, and from MT for January 2005 – January 2006 (one deployment) over the depth range ~0-564m. In this paper, we refer to each RaTS mooring deployment by its number within the sequence (1, 2 or 3), the timings of which are detailed in Table 1. A delay in the intended recovery and redeployment of the moorings in January 2006 led to a data gap of roughly three weeks in all sensors except the ADCPs, which had sufficient onboard data storage to allow uninterrupted collection up to recovery in mid-February. The MT mooring was lost during the second deployment, hence the collection of only one year of data at this site.

The moored CTDs, TDRs and TRs were manufactured by Richard Branckner Research (RBR) Ltd, and were configured to collect data at hourly intervals, whilst the 75kHz Workhorse Long Ranger ADCPs (RD Instruments) averaged data into 15-minute ensembles. At the RaTS site the RBR sensors were separated vertically by between 15 and 35m within the depth range expected to sample modified UCDW (below 200m). The upward-looking ADCP, at ~200m, measured the velocity profile of the upper water column with a vertical resolution of 4m and a velocity resolution of $1 mms^{-1}$. At MT, the upward looking ADCP (bin depth and velocity resolution as above), was located at ~115m, and the RBR sensors below ~185m at intervals of ~50-70m. Deployment depths and sample recording rates for each instrument are detailed in Table 2 **[insert Table 2 here]**.

The CTD profiles at the RaTS site were carried out roughly 1-2 times per week from January 2005 – April 2007, using a SeaBird Electronics SBE-19 instrument. Deployment was from a small boat during the summer and through the sea ice cover from a sledge during winter, given favourable ice conditions. Further details on data collection can be found in Meredith et al. (2004), Clarke et al (this issue) and Wallace (2007).

Surface meteorological data were obtained from Rothera Research Station, courtesy of the British Antarctic Survey. Hourly values of wind direction and speed were collected for three 30-day periods for the summer and winter of the first two RaTS mooring deployments and the summer of the third RaTS deployment. Linear interpolation was used to fill gaps in the wind time series, where not more than five consecutive data points were missing.

This analysis also makes use of the AntPen04.01 tide model (Padman, unpublished; www.esr.org/ptm_index), which is a high-resolution (1/30° longitude by 1/60° latitude, ~2km) forward model, based on the shallow water equations, and forced at the open boundary by tide heights from the circum-Antarctic forward model (CATS02.01; Padman et al., 2002) and by astronomical forcing. The model is tuned to data using a linear benthic drag coefficient.

4. Results

Internal waves are observed in our data from Marguerite Bay at both diurnal and semidiurnal tidal frequencies, in addition to quasi-periodic fluctuations on timescales of a few days. The latter longer-period fluctuations appear to be atmospherically-forced, and are investigated in Section 4.1, whilst the internal tides are explored in Section 4.2. Characteristic profiles of potential temperature, θ, S, potential density anomaly, σ_θ, and buoyancy frequency, N, from the RaTS site, along with a comparison of θ from the two mooring sites for the summers of 2005-2007 are shown in Figure 2 **[insert Figure 2 here]**, and will be referred to throughout the following analyses. N is derived from the gravitational acceleration, g, the reference density at depth z, ρ_0, and the vertical density gradient, $d\rho/dz$ (Pond & Pickard, 1983):

$$N(z) = \sqrt{\frac{-g}{\rho_0}\frac{d\rho}{dz}} \qquad (1)$$

4.1 Atmospherically-forced fluctuations

Figure 3 **[insert Figure 3 here]** shows T, S and σ_θ time series from the RaTS site, along with the horizontal velocity from the ADCP bin immediately below the surface, while Figure 4 **[insert Figure 4 here]** shows the corresponding T and ADCP data from the MT site. All time series are filtered using a 26-hour Butterworth lowpass filter to remove tidal and higher frequency variability. Markedly low variance in the ADCP data is indicative of the presence of sea ice above the mooring (e.g. Visbeck & Fischer, 1995; Hyatt et al., 2008) and shaded in grey on Figures 3 and 4. At the RaTS site in both 2005 and 2006 there were 3-4 weeks of ice cover, followed by 2-3 weeks of open water before the onset of pack ice. Ryder Bay may, in fact, be covered by fast ice for much of the winter, whilst the offshore regions of Marguerite Bay are covered in pack ice. Therefore, for simplicity, we will refer to all high concentration ice cover as 'pack ice'. We term periods interpreted as being pack ice covered as the 'ice-covered season', and periods of open water and those of brief ice cover the 'ice-free season'.

Quasi-periodic fluctuations on timescales of ~2-7 days have been observed in certain sections of the moored time series from the RaTS site (an example of the signal is marked by the grey oval on Figure 3), but are not observed at the MT mooring (Figure 4). Their signal is variable both in magnitude and duration, and is observed in all of the RaTS temperature loggers (CTDs, TR, TDR), although the magnitude of the signal decreases with depth, which is consistent with the lower gradients observed deeper in the water column (Figure 2). The fluctuations can also be seen in S and σ_θ at the uppermost CTD (199m), but are more difficult to identify in these time series at

274 the deeper sensors, due to lower signal-to-noise ratios compared with those in *T*
275 (Wallace, 2007). Thus, our analysis will concentrate upon *T* data. The thermohaline
276 properties of UCDW are relatively invariant (Hofmann & Klinck, 1998; Wallace,
277 2007), and at the RaTS site temperature below the WW minimum at the RaTS site
278 consistently increases with depth (Meredith et al., 2004; Wallace, 2007). Thus, for
279 this location, and for our specific purposes, isotherms can be considered analogous to
280 isopcynals in UCDW and *T* can reasonably be considered a proxy for σ_θ, allowing
281 more complete coverage of the water column than density time series would allow.
282
283 The fluctuations are apparently unaffected by the initial periods of ice cover, but are
284 smaller in magnitude in the presence of pack ice. A high degree of interannual
285 variability is also observed, with the fluctuations being most pronounced in Feb-Jun
286 during deployment 2 (2006). Although reduced during the ice-covered season, the
287 signal is clearly visible during 2006, whereas during 2005 it is difficult to distinguish
288 in the presence of ice. In 2007 the fluctuations only become apparent in March, after
289 the region has been ice-free for more than two months.
290
291 The temporal and spatial variability of the temperature fluctuations is best illustrated
292 by means of power spectral analysis, which partitions variance as a function of
293 frequency (Emery & Thompson, 2004). Figure 5a **[insert Figure 5 here]** shows
294 power spectral density (PSD) for all temperature sensors during the ice-free season of
295 deployment 2, when the fluctuations are observed most clearly. Several peaks are
296 consistently present at different depths over this frequency range, and the decrease in
297 variance with depth can be clearly observed. Hence, comparison between the different
298 deployments and between the two mooring sites (Figure 5b and 5c) requires the

299 selection of time series from similar depths. The instruments at 283m, 274m and
300 273m for the three RaTS deployments, respectively, and 298m for MT are most
301 appropriate for this. The spectra in Figures 5b and 5c show several features of note:
302 (1) variability in the 2-7 day band is consistently higher at the RaTS site than at MT;
303 (2) RaTS deployment 2 shows the strongest variability; and (3) the difference in
304 depths between the sensors is unlikely to be the most important factor in the observed
305 differences between the spectra, as the sensors from RaTS deployments 2 and 3 are at
306 virtually the same depth, yet show markedly different variability (i.e. the influence of
307 time is strong compared with that of depth). Figure 5d illustrates the difference
308 between the RaTS and MT sites, where spectra for each site, along with their 95%
309 confidence intervals, show that the RaTS site experiences stronger variability in the 2-
310 7 day band than is observed at MT. This is unlikely to arise from differences in
311 temperature gradients between the two sites, as they are virtually identical below
312 ~200m during the summers of 2005, 2006 and 2007 (Figure 2c). Finally, Figure 5e
313 illustrates the difference between the ice-free and ice-covered seasons for RaTS
314 deployment 2, such that variability in the 2-7 day band is clearly higher in the absence
315 of ice.
316
317 The ~2-7 day fluctuations are most readily interpreted as oscillations of isotherms,
318 and the broad frequency range of the oscillations indicates that they are forced by a
319 strongly variable mechanism operating on a timescale of several days. The most
320 obvious explanation for the observations is thus an oceanic response to wind forcing.
321 Supporting this concept, temperature anomaly time series over the ice-free season
322 correlate significantly with wind anomalies measured at Rothera, which are known to
323 differ from those elsewhere on the WAP because of local topography (Beardsley et

al., 2004). The oscillation is sensitive to wind direction, with the strongest correlation associated with northwest to southeastward winds. Correlations are positive with northwestward winds and negative with southeastward winds, indicating that the former lead to warming and the latter to cooling. Examples of the correlations are shown in Figure 6 **[insert Figure 6 here]** for the shallowest (CTD10822 at 202m) and deepest (CTD10824 at 286m) temperature sensors at the RaTS site for the 30-day period 26th January – 24th February 2005. The intervening three temperature sensors show similar correlations. Winds lead the temperature signal by 27-36 hours, and the correlations decrease with depth in the water column, from 0.56 at 202m to 0.36 at 286m. All correlations are significant at either the 95% or 99% level (statistical significance is calculated following the method of Trenberth, 1984). No significant correlations are observed during the ice-covered season, which is consistent with the observed decrease in the magnitude of the oscillation, indicating a seasonal cycle in the winds and/or the ocean's response to the atmospheric forcing. Spectral analysis of NW-SE winds from the ice-free season shows significant peaks over the 2-7 day period that correspond with those observed in temperature time series, as shown in Figure 7 **[insert Figure 7 here]** for deployment 2.

The significant lagged correlations with the winds are consistent with wind-driven upwelling and downwelling behaviour, whereby a northwestward wind (i.e. parallel to the coast; Figure 1b) tends to induce upwelling along the NE coast of Ryder Bay, leading to the observed temperature increase at depth, whilst a southeastward wind is associated with downwelling and a temperature decrease at depth. However, this simple correlation does not consider the cumulative response of the ocean to upwelling/downwelling favourable winds. For instance, Austin & Barth (2002) found

that an index of coastal upwelling/downwelling in the ocean off the coast of Oregon was a function of the weighted cumulative alongshore wind stress on a timescale of 2-8 days. Following their method, we examine the coastal upwelling response (i.e. the observed temperature fluctuations) to the cumulative NW-SE wind stress (W, positive NW-ward), weighted to the most recent observations, over the cumulative upwelling timescale (t_c), according to the equation:

$$W = \int_{t'=0}^{t} \tau^s e^{(t'-t)/t_c} dt' \quad (2)$$

where τ^s is the NW-SE wind stress and t' is time. The analysis is carried out over three 30-day periods for the ice-free and ice-covered season of each deployment (Table 3) **[insert Table 3 here]**. As previously, wind and oceanographic time series are filtered using a 26-hour Butterworth lowpass filter prior to analysis. Correlation of temperature time series with W for a number of different values of t_c reveal that upwelling/downwelling behaviour at the RaTS site responds to the cumulative NW-SE wind stress over a timescale of 17-90 hours. These results are in conceptual agreement with those of Austin & Barth (2002). Fewer significant correlations are observed during the ice-covered season, and possible explanations for this include: (1) seasonal changes in stratification, leading to a change in the ocean's response to wind forcing; (2) a seasonal cycle in the wind forcing; and (3) damping of the ocean's response to the atmosphere by the presence of sea ice. Each of these possibilities is discussed in turn.

(1) Figure 2 shows that buoyancy frequency is relatively stable below ~200m throughout the year, with only a small reduction in N during winter. This pattern is observed every year, and N is similar at these depths throughout the three deployments, yet the fluctuation clearly varies on both seasonal and interannual timescales. Figure 8 **[insert Figure 8 here]** shows time series of monthly mean NW-SE wind stress anomaly, buoyancy frequency anomaly at each of the sensor depths (derived from the RaTS CTD profile dataset) and t_c for significant correlations between each temperature sensor and the cumulative NW-SE wind stress. Significant correlations with cumulative wind stress are observed at all depths in the presence of both high and low N, so although we can expect the observed temporal variability of the fluctuations to be influenced by changes in stratification, the observations cannot be solely attributed to this cause.

(2) The time series of wind stress anomaly in Figure 8 shows that winds are generally stronger during the ice-covered season, which does not explain the observed temporal variability in the temperature fluctuations. Furthermore, significant correlations occur between temperature and NW-SE wind stress both when winds are anomalously strong and when they are anomalously weak, so the observations cannot be explained in terms of wind stress variability alone.

(3) Periods of sea ice cover are marked on Figure 8. In the presence of ice, the number of significant correlations is reduced, implying that the sea ice has a significant effect upon the transmission of wind stress to the deep ocean. This concept is supported by the rapidity of the response of the fluctuations to the presence of sea ice. Observations from Rothera Station suggest that sea ice

cover was more fragmented in Ryder Bay in 2006 than 2005, which is consistent with the relative strengths of the fluctuations during the two winters. Whether the decrease in the fluctuations during the ice-covered season is a response to local sea ice conditions in Ryder Bay or those throughout the wider Marguerite Bay area cannot be determined without comprehensive, high resolution sea ice data across the region. Ryder Bay can be covered with fast ice whilst the ice in the rest of northern Marguerite Bay is fragmented, or *vice versa*, but several years' worth of data from both locations would be needed, along with comprehensive sea ice observations, to unravel such connections.

The internal Rossby radius of deformation (r) sets the offshore length scale over which the influence of coastal upwelling is discernible. This can be estimated for the RaTS site via (from Emery & Thomson, 2004):

$$r = \frac{NH}{|f|} \tag{3}$$

where a water depth of H = 520m and a buoyancy frequency of $N = 2.1\times10^{-4}$ s^{-1} (which is the maximum value observed within UCDW) yields r = 8km. The RaTS site lies ~2km from the NE coast of Ryder Bay, and is, therefore, well within one internal Rossby radius of the coast, whereas the MT mooring lies ~15km, more than an internal Rossby radius, from the nearest coastline.

When an upwelled density structure intersects the surface as an upwelling front, this front can be driven arbitrarily far offshore by sustained winds (Allen et al., 1995;

422 Austin & Lentz, 2002), so the scale of upwelling influence is no longer set by the
423 internal Rossby radius. In the present case, it is presumed that upwelling influence
424 does remain within an internal Rossby radius of the coast for a number of reasons: we
425 consider temperature levels that are in excess of 115 m deep at the mooring sites,
426 winds that are highly variable, and an upwelling response that is expected to vary
427 greatly depending on the local orientation of the coastline. In this setting, it seems
428 unlikely that upwelling would be sufficiently sustained to bring these isotherms to the
429 surface nearshore.
430
431 The lack of a clear upwelling signal at MT may be explained in two ways: (1) the
432 upwelling influence is trapped within an internal Rossby radius of the coastline, and
433 so does not extend to MT; (2) winds at Rothera are known to differ from those in
434 other areas of Marguerite Bay (Beardsley et al., 2004), so the correlation of
435 temperature records from the RaTS site with Rothera winds may suggest that this
436 upwelling behaviour is a relatively local phenomenon, which cannot therefore be
437 expected to influence localities such as MT. Further investigation of this spatial
438 variability would require data from several locations around Marguerite Bay.
439
440 The temporal variability of the quasi-periodic fluctuations is best investigated by
441 comparison of the total variance, σ^2, over the 2-7 day period for each temperature
442 sensor (Figure 9) **[insert Figure 9 here]**. σ^2 of 114-day time series, limited by the
443 length of deployment 3, is shown for the ice-free and ice-covered seasons of each
444 RaTS deployment, and values for the two seasons from the different deployments are
445 compared in Table 4 **[insert Table 4 here]**. In the shallowest two instruments, σ^2 is
446 ~3-4 times as large during the ice-free season as in the presence of ice for both

447 deployments 1 and 2. The difference in σ^2 between the ice-free and ice-covered
448 seasons becomes less pronounced in the deeper instruments during deployment 1, but
449 remains at a factor of ~3-4 during deployment 2 at all depths. Values from the ice-free
450 season of deployment 2 are ~2-8 times larger than those of deployments 1 and 3,
451 whilst during the ice-covered season, values of σ^2 from deployment 2 are ~2-3 times
452 larger than those from deployment 1.
453
454 Coastal upwelling involves both vertical and horizontal motion of the water column,
455 thus the fluctuations observed at the RaTS site can be expected to arise from both
456 vertical and lateral temperature gradients. Whilst our data from just two locations are
457 not sufficient to fully determine the relative importance of horizontal and vertical
458 water motions in generating the temperature fluctuations, it is possible to estimate the
459 magnitude of the vertical perturbations of the water column that would be required to
460 generate the observed fluctuations, thereby providing a realistic upper limit for the
461 amplitude of the coastal upwelling response. The depth perturbation, D', is calculated
462 from the representative temperature gradient, $\partial T_{CTD} / \partial z$, at depth z, and the magnitude
463 of the temperature fluctuation, T'_m, measured at the mooring:
464
465 $$D' = \frac{T'_m}{\partial T_{CTD} / \partial z} \quad (4)$$
466
467 such that a typical temperature perturbation of 0.3˚C at 200m (during the ice-free
468 season), with an average temperature gradient of 0.011˚C/m over the depth range 195-
469 205m, yields D' = 27m. Deeper sensors experience smaller temperature

perturbations, but the associated temperature gradients are also smaller, so values of D' are comparable between the different depths.

In summary, the quasi-periodic fluctuations observed at the RaTS site are a manifestation of coastal upwelling (downwelling) leading to a temperature increase (decrease) within the modified UCDW below ~200m depth. These oscillations are primarily driven by NW-SE-ward winds that induce upwelling/downwelling along the NE coast of Ryder Bay, ~2km from the RaTS site. The ocean's response to the wind forcing has the potential to generate vertical perturbations of the water column of the order of several metres to a few tens of metres, and is damped in the presence of pack ice.

4.2 Internal tides

4.2.1 Quantification of the barotropic tide

When considering internal tides using subsurface measurements, it is important to be able to distinguish, and quantify the influence of, the barotropic tide. Here we use the AntPen04.01 tidal model (Padman, unpublished; www.esr.org/ptm_index) to estimate barotropic tides at both moorings locations. The tides in this region are relatively small, with velocities of $\leq 3.24 cms^{-1}$ at the RaTS site and $\leq 0.59 cms^{-1}$ at MT for the dominant diurnal (O1, K1) and semidiurnal (M2, S2) constituents (see Table 5) **[insert Table 5 here]**. At the RaTS site, the velocities of the semidiurnal tides are roughly twice those of the diurnal tides. The M2 and S2 semidiurnal tides, and the O1 diurnal tide, are dominated by the northward component of flow, whilst the K1 diurnal tide is dominated by the eastward component of flow. In contrast, the tidal

energy is more evenly distributed between the diurnal and semidiurnal constituents at MT, and all constituents detailed here are dominated by the eastward component of flow, although this dominance is weaker in the S2 and K1 tides.

As can be seen on Figure 1, the RaTS site is located in an elongated basin oriented roughly E-W, whilst the MT site lies in a trough running NE-SW. Thus, the tidal energy available for the generation of baroclinic tides is likely to differ between the two sites, not only due to differences in the barotropic forcing, but also due to the respective orientations of the barotropic tides relative to the seabed topography.

4.2.2 Internal tides in the moored velocity records

Spectra of velocity data using 112-day time series from the moored upward-looking ADCPs at both mooring sites clearly show energy at tidal frequencies (Figure 10) **[insert Figure 10 here]**. Spectra from the RaTS site show relatively strong diurnal tides in eastward velocity (u), whilst the semidiurnal tides are virtually absent, despite the stronger semidiurnal barotropic forcing detailed in Table 5. All tidal signals in northward velocity (v) are weak, despite stronger barotropic forcing in v than u for the M2, S2 and O1 constituents. Both seasonal and interannual variability are observed, with stronger tidal signatures during the ice-free season, and lower tidally-induced variance during deployment 3 compared with the other deployments. During the ice-free season, distinct changes in the strength of the diurnal tidal peaks are observed with depth, with PSD(u) from all three deployments showing a distinctive pattern of relatively high PSD close to the surface and below ~90m, and a band of low values centred at ~50m. This is highlighted in Figure 11 **[insert Figure 11 here]**, which shows spectra and confidence intervals for u and v at selected depths.

520

521 At MT, the energy at diurnal frequencies is comparable to that at the RaTS site, whilst
522 that at semidiurnal frequencies is significantly higher, despite the diurnal barotropic
523 forcing being comparable to the M2 semidiurnal forcing. The energy at the
524 semidiurnal frequencies is likely subject to contributions from the observed strong,
525 near-inertial energy (*f* is very close to the frequencies of the semidiurnal tides at this
526 latitude). However, non-tidal near-inertial currents would be expected to generate a
527 broad peak in PSD, whereas the M2 and S2 peaks are well defined, indicating that the
528 semidiurnal tidal energy is indeed strong compared with the diurnal energy. The
529 diurnal tides also show slightly higher flow in *v* than *u*, despite marginally stronger
530 barotropic forcing in the eastward component of flow. The energy associated with the
531 O1, K1 and M2 tidal frequencies changes with depth, particularly during the ice-free
532 season, where they decrease to roughly zero between 50 and 100m, but there is no
533 increase in energy at depth analogous to that observed at the RaTS site. Selected
534 spectra (and confidence intervals) from MT are also shown in Figure 11.
535

536 To summarise, velocity data recorded at the two mooring sites show tidal signals that
537 differ from both their respective barotropic forcings and from each other, and the
538 strength of the tidal signals changes with depth at both mooring sites. The particularly
539 strong semidiurnal energy at MT is likely to be influenced by near-inertial currents of
540 non-tidal origin, with particularly strong semidiurnal tidal currents also present.
541 During the ice-free period, other frequencies (from ~0.5 to 2.0 cpd) also show
542 surface-intensified energies at MT, and their absence during the ice-covered periods is
543 strongly suggestive of atmospheric processes being responsible. (This range of
544 frequencies includes the diurnal tidal band, explaining the surface-intensification of

545 diurnal tidal energy during the ice-free months at MT). In contrast, the RaTS site does
546 not experience significant near-inertial energy, and whilst there is evidence of higher
547 energies in the near-surface layers during the ice-free months, the observed depth-
548 dependence of the diurnal tidal energy cannot be explained solely by atmospheric
549 forcing covering a range of frequencies that includes the diurnal band. In particular,
550 the energy at diurnal frequencies does not consistently decrease away from the
551 surface, but instead shows a relative minimum in energy at around 50m. This is
552 consistent with the presence of internal (baroclinic) tides at the RaTS site.
553
554 The tidal currents show distinct interannual variability and are generally reduced
555 during the ice-covered season, which can be attributed in part to temporal changes in
556 stratification (Figure 2). However, both seasonal and interannual changes in N are of
557 the same order of magnitude ($\sim 10^{-3} s^{-1}$), yet seasonal variability in PSD is clearly far
558 stronger than interannual variability, so the observed changes cannot be attributed to
559 variability in N alone. Given that the barotropic forcing is not expected to show strong
560 temporal variability, the decrease in tidal currents in the presence of ice indicates the
561 existence of a potentially important relationship between tides and sea ice, which is
562 worthy of further investigation. Another likely influence upon baroclinic tidal flow is
563 low frequency current variability (Wallace, 2007), which, by altering the background
564 density field and introducing background shears, can influence the pathways along
565 which internal wave energy travels, and thus the manner in which it interacts with
566 bathymetry (Sherwin & Taylor, 1990).
567
568 To confirm the presence of internal tides we conducted harmonic analysis of ADCP
569 current data using the Matlab package T_TIDE (Pawlowicz et al., 2002). Figure 12

570 **[insert Figure 12 here]** shows profiles of tidal phase extracted for the O1, K1, M2
571 and S2 tides at the RaTS site and MT. Phase shifts of 180˚, characteristic of internal
572 tides (Gill, 1982), are observed at the RaTS site, whilst no such phase shifts occur at
573 MT. However, it is necessary to consider that the MT ADCP samples the upper
574 ~100m of a water column that is >800m deep, so the lack of phase change measured
575 at this location does not necessarily indicate the absence of internal tides. The RaTS
576 data show a larger number of 180˚ phase changes for the semidiurnal than the diurnal
577 constituents, but due to the low tidal energy at the semidiurnal frequencies at this site,
578 and the associated difficulties of relating phase information to the observed
579 variability, the following discussion will concentrate upon the diurnal tides during the
580 ice-free season, and in particular the eastward component of flow.
581
582 The phase profiles at the RaTS site highlight three primary regimes of variability over
583 the depth profiles: (1) relatively high variability above ~40m, characterised by 180˚
584 phase shifts in O1 and K1 of deployment 2, and O1 of deployment 3; (2) low
585 variability between ~40 and ~100-120m, characterised by virtually constant phase;
586 and (3) high variability below ~100-120m, characterised by between one and ten 180˚
587 phase changes. These phase changes indicate regions of high shear and correspond
588 well with the near-surface and deep regions of high energy shown in *u* in Figure 10,
589 and/or the transitions between regions of high and low energy, whilst the relatively
590 stable phase profile between ~40 and ~100-120m corresponds well with the low
591 energy observed at these depths. However, the relatively constant phase throughout
592 the shallow water column for O1 and K1 of deployment 1, and K1 of deployment 3,
593 indicates that relatively large changes in PSD with depth need not be associated with
594 current reversals.

595

596 Profiles of diurnal tidal amplitude are also in good agreement with the results from the
597 RaTS PSD analysis (Figure 13a-c) **[insert Figure 13 here]**, with the lowest
598 amplitudes observed where PSD is lowest. This change in tidal amplitude with depth
599 is also indicative of baroclinic tides (a barotropic tide should not show such
600 variability), confirming their importance at the RaTS site. Amplitude profiles from
601 MT (Figure 13d) also show a decrease with depth, particularly at the semidiurnal
602 frequencies, which is again consistent with the observed patterns in PSD. This
603 indicates that, even though no phase change is observed at this location, the site is
604 influenced by internal tides.

605

606 *4.2.3 Generations sites of internal tides*

607 The inconsistencies between the expected and observed relative strengths of the
608 eastward and northward components of tidal flow at the RaTS site suggest that the
609 orientation of the flow with respect to seabed topography is important. The location of
610 Marguerite Bay poleward of the critical latitude for diurnal internal tides, but
611 equatorward of that for semidiurnal internal tides, implies that the superinertial
612 semidiurnal signal should be allowed to propagate freely (although it may be locally
613 generated), whilst we expect the subinertial diurnal internal tide to be generated in the
614 region of our moorings or to have propagated along the coastline or local bathymetric
615 slope with an offshore or off-slope horizontal length scale of the order of the internal
616 Rossby radius. The strong diurnal internal signal at the RaTS site is thus consistent
617 with its proximity to the coast.

618

Internal tides have been observed in the Arctic (e.g. Konyaev et al., 2000; Morozov et al., 2003) and around the margins of Antarctica (e.g. Foldvik et al., 1990; Levine et al., 1997; Albrecht et al., 2006), and both models (e.g. Morozov & Pisarev, 2002; Padman et al., 2006) and observational work (e.g. Albrecht et al., 2006) suggest that the interaction of barotropic flows with seabed topography is an important process in the generation and propagation of internal tides. In order to identify potential generation sites in the vicinity of the two mooring sites we derive the internal tidal forcing function, F, after Sherwin (1988):

$$F = \frac{izQN^2}{\omega}\nabla\left(\frac{1}{H}\right) \tag{5}$$

where Q is the tidal flow (defined as uH, vH, where u, v are the eastward and northward velocities and H the water depth), ω is the frequency of the internal tide, z is the depth of interest and $\nabla\left(\frac{1}{H}\right)$ is the horizontal gradient of the inverse of the water depth. Bathymetry data are from the US SO-GLOBEC program (www.whoi.edu/science/PO/so_globec/WHOI_tech_report) and are used internally in AntPen04.01 to calculate uH and vH across the regions around each mooring site marked in Figure 1. The calculation is carried out for both the ice-free and ice-covered seasons of all years at the RaTS site, but results are shown here for 2006 only. Deployments 1 and 3 show results consistent with those presented here. Average profiles of N are calculated for the ice-free and ice-covered seasons from CTD profiles collected from February-June 2006 and July-November 2006, respectively. The analysis is carried out for both the K1 and M2 internal tides, in order to permit comparison of the potential local generation sites for both diurnal and semidiurnal

643 internal tides. F^* is also calculated for the K1 and M2 tides during the ice-free season
644 at MT, using a profile of N derived from a CTD cast carried out at this location during
645 February 2006. In the absence of winter CTD profiles at this location, F^* cannot be
646 calculated for the ice-covered season.
647
648 Figure 14a-d **[insert Figure 14 here]** shows depth-integrated tidal forcing function,
649 F^*, for the region around the RaTS site marked on Figure 1. For both tidal
650 constituents, values of F^* are of the order of 1-2 Nm^{-2} over much of the domain but
651 can be >50 Nm^{-2} over areas of rugged bathymetry. At MT (Figure 14e-f), F^* is
652 generally higher, particularly for K1, with values of ~10 Nm^{-2} over much of the
653 region and, again >50 Nm^{-2} over areas of rugged bathymetry. These results echo those
654 of Sherwin (1988) and Sherwin & Taylor (1990), who studied internal tides generated
655 over the region of the Malin Shelf, north of Ireland. Sherwin & Taylor (1990) derived
656 the highest values of F^* ($\leq$ 60 Nm^{-2}) at the continental shelf break and values of ~10-
657 20 Nm^{-2} over the continental slope. The results of Sherwin (1988) were similar, with
658 values of $F^* \leq 40$ Nm^{-2} at the shelf break and, again, ~10-20 Nm^{-2} over the
659 continental slope, and he concluded that both regions were important for the
660 generation of the observed internal tides.
661
662 The similarity of F^* derived for the Malin Shelf and Marguerite Bay is worthy of
663 note, given that N measured on the Malin Shelf was roughly twice that in Marguerite
664 Bay and the tidal forcing of the North Atlantic is an order of magnitude larger than
665 that on the WAP (Sherwin 1988). We therefore conclude that the rugged nature of the
666 WAP bathymetry, as reflected in $\nabla\left(\frac{1}{H}\right)$, has the potential to induce relatively strong
667 baroclinic tides, despite the weak barotropic forcing and weak stratification.

668

669 Potential generation sites for the diurnal internal tide observed at the RaTS site are the
670 NE coastline and around the small islands to the SW side of Ryder Bay. Values of F^*
671 are slightly higher over the region for the M2 internal tide due to larger values of Q
672 (see details of tidal current flow in Table 5), although this is offset in part by the
673 increase in ω, and lower during the ice-covered season for both tidal constituents due
674 to reduced stratification. However, given the similarities between the four maps, the
675 influences of Q, N and ω are clearly small compared to that of the bathymetry. Maps
676 of F^* for the eastward and northward components of flow are not shown separately
677 here, but vH accounts for ~69% of the diurnal Q and ~75% of the semidiurnal Q.
678 Thus, the observed temporal variability in PSD, the differences between PSD of the
679 diurnal and semidiurnal constituents, and the marked dominance of PSD(u) over
680 PSD(v) cannot be solely attributed to differences in internal tide generation sites, or
681 orientation of the tidal flow with respect to the known bathymetry.

682

683 At MT, most of the potential generation sites are located around the northern and
684 western margins of the trough in which the mooring lies. The areas of high F^* (>20
685 Nm^{-2}) are similar for both the diurnal and semidiurnal constituents, but the higher
686 value of ω for the semidiurnal tide leads to a clear decrease in F^* over much of the
687 domain. In contrast to the RaTS site, uH dominates Q, accounting for ~61% of the
688 diurnal Q and ~67% of the semidiurnal Q. Given that u and v are similar for K1, this
689 shows that the orientation of the tidal flow with respect to the topography is an
690 important factor.

691

692

5. Discussion

This study has shown that northern Marguerite Bay is affected by internal tides, although their nature differs between the nearshore RaTS site and the offshore MT site. At the RaTS site, energy at the diurnal frequencies dominates over the semidiurnal energy, despite stronger barotropic forcing at semidiurnal frequencies. The orientation of the tidal flow with respect to seabed topography is also important, with higher energy observed in the eastward component of tidal flow for both the O1 and K1 internal tides, despite O1 being subject to stronger northward barotropic flow. An investigation of internal tide generation sites around Ryder Bay also indicates that the northward component of flow has more potential for generating internal tides, due to its orientation with respect to bathymetric features. However, observations show stronger tidal flow in the eastward direction, implying that the relationship between the forcing and propagation of the internal tides is complex. In addition, the RaTS site is influenced by quasi-periodic temperature fluctuations that we have shown are due to local wind-forced coastal upwelling and downwelling.

At MT, tidal energy is far stronger at the semidiurnal frequencies than the diurnal frequencies, despite similar barotropic forcing. Atmospherically-forced signals are observed to contribute to the energy at both the diurnal and semidiurnal frequencies, but the signatures of the baroclinic tides can still be observed in the upper water column. Again, the orientation of tidal flow with respect to seabed topography is important, with the eastward component of flow having the strongest potential for internal tide generation.

There are a number of possible explanations for the temporal variability of both the atmospherically and tidally-forced signals. The most likely are: (1) changes in stratification, whereby stronger stratification leads to a stronger internal wave signal due to higher variance at the depth of interest; (2) changes in background vertical shear arising from low frequency current variability; and (3) changes in sea ice conditions, which appear to affect tidal flow and have the potential to influence the atmospherically-forced signal, such that ice thickness, coherence and ridging can influence the transmission of wind-forcing to the ocean (e.g. Steele et al., 1989; Andreas et al., 1993; McPhee et al., 1999).

Considering each of these possibilities in turn:

(1) Changes in stratification undoubtedly influence the temporal variability of both the atmospherically-forced and baroclinic tidal flows. However, it has been demonstrated that neither seasonal nor interannual changes in stratification can account for all of the variability in either the atmospherically-forced signal or the internal tides.

(2) Seasonal and interannual changes in low frequency currents have been observed in the uppermost 200m of the water column at the RaTS site (Wallace, 2007) and are likely to account for some of the changes in internal tidal activity that are not related to stratification. There are, however, currently insufficient data for a full investigation of this theory.

(3) The rapid response and decay of the atmospherically-forced signal to the onset of pack ice clearly indicates that sea ice conditions have an important influence upon the oscillations. Observations from Rothera Research Station suggest that the ice was more fragmented during the winter of 2006 than 2005, which is consistent with the continuation of the (albeit weakened) oscillation throughout the ice-covered season of 2006. More detailed ice data (including thickness, degree of ridging etc) are required to assess further the dynamical role of ice in suppressing atmospherically-forced oscillations. The seasonal variability in the tidal energy at the RaTS site is likely linked to sea ice conditions, but the nature of this connection is as yet unclear.

6. Conclusions

We conclude that internal perturbations in northern Marguerite Bay are subject to a number of influences, including local winds, sea ice, barotropic tides and stratification. The observed internal wave and coastal upwelling activity may contribute to vertical mixing and nutrient distribution in Ryder Bay, with potential consequences for the operation of the local ecosystem; this is thus worthy of further investigation. The presence of a wind-driven signal beneath the permanent pycnocline at the RaTS site indicates that the UCDW is, locally at least, subject to some degree of atmospheric forcing, implying that changes in sea ice cover or atmospheric circulation could have implications for mixing processes in these deep waters. The absence of the wind-driven signal at the MT site demonstrates that Ryder Bay is subject to at least some different forcing mechanisms to those of the more open waters of Marguerite Bay, as does the difference in the internal tidal signals between the two locations. The

RaTS programme is continuing in Ryder Bay, and we are planning to redeploy our fixed moorings within the next few years, including deployments at other sites within Marguerite Bay and on the broader WAP shelf. This will allow us to quantify better the roles of the processes elucidated above, and to assess the local impacts of the internal waves and coastal upwelling on the marine ecosystem.

Acknowledgements

We would like to thank personnel at the British Antarctic Survey's Rothera Research Station, particularly the Marine Assistants and boatmen, without whom the collection of RaTS CTDs since 1998 would not have been possible. Thanks also to the scientists and crew aboard the RRS *James Clark Ross* and the RV *Laurence M Gould*, and to the mooring technicians from the National Oceanography Centre, Southampton, for all their help and hard work. Many thanks to Bob Beardsley for providing the SO-GLOBEC data used here, the Proudman Oceanographic Laboratory for the Rothera tide gauge data and Laurie Padman for the AntPen04.01 model data. Thanks also to Carlos Moffat and an anonymous reviewer for positive and constructive feedback on this paper. The Rothera Time Series, Marguerite Bay moorings and Margaret Wallace's PhD studentship were funded by the Natural Environment Research Council in the AFI Scheme, grant number NER/S/S/2004/13013.

792 References

793 Albrecht, N., Vennell, R., Williams, M., Stevens, C., Langhorne, P., Leonard, G. and
794 Haskell, T., 2006. Observation of sub-inertial internal tides in McMurdo Sound,
795 Antarctica. Geophysical Research Letters 33, L24606, doi:10.1029/2006GL027377.
796 Allen, J. S., Newberger, P.A., Federiuk, J., 1995. Upwelling circulation on the Oregon
797 continental shelf. Part I: Response to idealized forcing. Journal of Physical
798 Oceanography 25, 1843-1866.
799 Andreas, E. L., Lange, M.A., Ackley, S.F., Wadhams, P., 1993. Roughness of
800 Weddell sea ice and estimates of the air-ice drag coefficient. Journal of Geophysical
801 Research 98 (C7), 12439-12452.
802 Austin, J. A. and Barth, J.A., 2002. Variation in the position of the upwelling front on
803 the Oregon shelf. Journal of Geophysical Research 107 (C11), 3180,
804 doi:10.1029/2001JC000858.
805 Austin, J. A., Lentz, S.J., 2002. The inner shelf response to wind-driven upwelling
806 and downwelling. Journal of Physical Oceanography 32, 2171-2193.
807 Beardsley, R. C., Limeburner, R. and Owens, W.B., 2004. Drifter measurements of
808 surface currents near Marguerite Bay on the western Antarctic Peninsula shelf during
809 austral summer and fall, 2001 and 2002. Deep-Sea Research II 51, 1947-1964.
810 Dinniman, M. S. and Klinck, J.M., 2004. A model study of circulation and cross-shelf
811 exchange on the west Antarctic Peninsula continental shelf. Deep-Sea Research II 51,
812 2003-2022.
813 Clarke, A., Meredith, M.P., Wallace, M.I., Brandon, M.A. and Thomas, D.N., in
814 press. Seasonal and interannual variability in temperature, chlorophyll and
815 macronutrients in Ryder Bay, northern Marguerite Bay, Antarctica. Deep-Sea
816 Research II, PAL-LTER Special Issue.

817 Costa, D.P. and Crocker, D.E., 1996. Marine mammals of the Southern Ocean. In:
818 Ross, R.M., Hofmann, E.E., Quetin, L.B. (Eds.), Foundations for Ecological Research
819 West of the Antarctic Peninsula, Antarctic Research Series 70. AGU, Washington,
820 D.C., pp. 287-301.
821 Dinniman, M. S., Klinck, J.M., 2004. A model study of circulation and cross-shelf
822 exchange on the west Antarctic Peninsula continental shelf. Deep-Sea Research II 51,
823 2003-2022.
824 Emery, W. J. and Thomson, R.E., 2004. Data Analysis Methods in Physical
825 Oceanography. Elsevier, Amsterdam.
826 Foldvik, A., Middleton, J. and Foster, T., 1990. The tides of the southern Weddell
827 Sea. Deep-Sea Research 97, 1345-1362.
828 Fraser, W.R. and Trivelpiece, W.Z., 1996. Factors controlling the distribution of
829 seabirds: winter-summer heterogeneity in the distribution of Adélie penguin
830 populations. In: Ross, R.M., Hofmann, E.E., Quetin, L.B. (Eds.), Foundations for
831 Ecological Research West of the Antarctic Peninsula, Antarctic Research Series 70.
832 AGU, Washington, D.C., pp. 257-272.
833 Gill, A. E., 1982. Atmosphere-Ocean Dynamics. International Geophysics Series 30.
834 Academic Press, San Diego, California.
835 Gregg, M. C., 1987. Diapycnal mixing in the thermocline: a review. Journal of
836 Geophysical Research 92 (C5), 5249-5286.
837 Halpern, D., 1976. Structure of a coastal upwelling event observed off Oregon during
838 July 1973. Deep-Sea Research 23, 495-508.
839 Hofmann, E. E. and Klinck, J.M., 1998. Thermohaline variability of the waters
840 overlying the West Antarctic Peninsula Continental Shelf. In: Jacobs, S., Weiss, R.

841 (Eds.), Oceans, Ice and Atmosphere: Interactions at the Antarctic Continental Margin,
842 Antarctic Research Series 75. AGU, Washington, D.C., pp. 67-81.
843 Howard, S. L., Hyatt, J., Padman, L., 2004. Mixing in the pycnocline over the western
844 Antarctic Peninsula shelf during Southern Ocean GLOBEC. Deep-Sea Research II 51,
845 1965-1979.
846 Hyatt, J., Visbeck, M., Beardsley, R., Owens, W.B., 2008. Measurements of sea ice
847 properties using a moored upward-looking acoustic Doppler current profiler (ADCP).
848 Deep-Sea Research II 55, 351-364.
849 Intergovernmental Oceanographic Commission of UNESCO (IOC), 2006. Manual on
850 sea-level measurements and interpretation, volume IV: an update to 2006. IOC
851 Manuals and Guides IV (14), JCOMM Technical Report No. 31; WMO/TD. No.1339,
852 56 pp.
853 Klinck, J. M., 1998. Heat and salt changes on the continental shelf west of the
854 Antarctic peninsula between January 1993 and January 1994. Journal of Geophysical
855 Research 103 (C4), 7617-7636.
856 Klinck, J. M., Hofmann, E.E., Beardsley, R.C., Salihoglu, B. and Howard, S., 2004.
857 Water-mass properties and circulation on the west Antarctic Peninsula Continental
858 Shelf in Austral Fall and Winter 2001. Deep-Sea Research II 51, 1925-1946.
859 Koentopp, M., Eisen, O., Kottmeier, C., Padman, L., Lemke, P., 2005. Influence of
860 tides on sea ice in the Weddell Sea: investigations with a high-resolution dynamic-
861 thermodynamic sea ice model. Journal of Geophysical Research 110 (C02014), 137-
862 158.
863 Konyaev, K. V., 2000. Internal tide at the critical latitude. Izvestiya, Atmospheric and
864 Oceanic Physics 36 (3), 363-375.

865 Konyaev, K. V., Plueddemann, A. and Sabinin, K.D., 2000. Internal tide on the
866 Yermak Plateau in the Arctic Ocean. Izvestiya, Atmospheric and Oceanic Physics 36
867 (4), 542-552.
868 Kowalik, Z. and Proshutinsky, A.Y., 1994. The Arctic Ocean tides. In: Johansse,
869 O.M., Muench, R.D., Overland, J.E. (Eds.), The Polar Oceans and their role in
870 shaping the Global Environment, Geophysical Monograph 85. AGU, Washington,
871 D.C., pp. 137-158.
872 LeBlond, P., Mysak, L.A., 1978. Waves in the ocean. Elsevier Oceanographic Series
873 20. Elsevier, Amsterdam.
874 Levine, M. D., Padman, L., Muench, R.D. and Morison, J.H., 1997. Internal waves
875 and tides in the western Weddell Sea: Observations from Ice Station Weddell. Journal
876 of Geophysical Research 102 (C1), 1073-1089.
877 Mackinnon, J. A. and Gregg, M.C., 2005. Spring mixing: turbulence and internal
878 waves during restratification on the New England shelf. Journal of Physical
879 Oceanography 35, 2425-2443.
880 Martinson, D.G., Stammerjohn, S.E., Iannuzzi, R.A. and Smith, R.C. in press. Palmer,
881 Antarctica, Long-term Ecological Research Program first twelve years: Physical
882 oceanography, spatio-temporal variability. Deep-Sea Research II, PAL-LTER Special
883 Issue.
884 McPhee, M. G., Kottmeier, C., Morison, J.H., 1999. Ocean heat flux in the central
885 Weddell Sea during winter. Journal of Physical Oceanography 29, 1166-1179.
886 Meredith, M. P., Renfrew, I.A., Clarke, A., King, J.C. and Brandon, M.A., 2004.
887 Impact of the 1997/98 ENSO on upper ocean characteristics in Marguerite Bay,
888 western Antarctic Peninsula. Journal of Geophysical Research 109, 9013-9032.

889 Mitchum, G. T., Clarke, A.J., 1986. The frictional nearshore response to forcing by
890 synoptic scale winds. Journal of Physical Oceanography 16, 934-946.
891 Morozov, E. G. and Pisarev, S.V., 2002. Internal tides at the Arctic latitudes
892 (numerical experiments). Oceanology 42 (2), 165-173.
893 Morozov, E. G., Pisarev, S.V., Neiman, V.G. and Erofeeva, S.Y., 2003. Internal tidal
894 waves in the Barents Sea. Doklady Earth Sciences 393 (8), 686-688 (translated from
895 Russian).
896 Muench, R. D., Padman, L., Howard, S.L., Fahrbach, E., 2002. Upper ocean
897 diapycnal mixing in the northwestern Weddell Sea. Deep-Sea Research II 49, 4843-
898 4861.
899 Munk, W. and Wunsch, C., 1998. Abyssal recipes II: energetics of tidal and wind
900 mixing. Deep-Sea Research I 45, 1977-2010.
901 New, A. L., 1988. Internal tidal mixing in the Bay of Biscay. Deep Sea Research 35
902 (5), 691-709.
903 New, A. L. and Pingree, R.D., 1990. Evidence for internal tidal mixing near the shelf
904 break in the Bay of Biscay. Deep Sea Research 37 (12), 1783-1803.
905 Ostrovsky, I., Yacobi, Y.Z., Walline, P. and Kalikhman, I., 1996. Seiche-induced
906 mixing: Its impact on lake productivity. Limnology and Oceanography 41 (2), 323-
907 332.
908 Padman, L., Fricker, H. A., Coleman, R., Howard, S., Erofeeva, L., 2002. A new tide
909 model for the Antarctic ice shelves and seas. Annals of Glaciology 34, 247-254.
910 Padman, L., Howard, S., Muench, R., 2006. Internal tide generation along the South
911 Scotia Ridge. Deep Sea Research II: Topical Studies in Oceanography 53, 157-171.

912 Pawlowicz, R., Beardsley, B. and Lentz, S., 2002. Classical tidal harmonic analysis
913 including error estimates in MATLAB using T_TIDE. Computers and Geoscience,
914 28, 929-937.
915 Polzin, K. L., Toole, J.M., Ledwell, J.R. and Schmitt, R.W., 1997. Spatial variability
916 of turbulent mixing in the abyssal ocean. Science 276, 93-96.
917 Pond, S. and Pickard, G.L., 1983. Introductory dynamical oceanography, 2nd Edition.
918 Pergamon Press, Oxford.
919 Rippeth, T. P. and Inall, M.E., 2002. Observations of the internal tide and associated
920 mixing across the Malin Shelf. Journal of Geophysical Research 107 (C4), 8687-
921 8705.
922 Ross, R.M., Quetin, L.B. and Lascara, C.M. (1996a). Distribution of Antarctic krill
923 and dominant zooplankton west of the Antarctic Peninsula. In: Ross, R.M., Hofmann,
924 E.E., Quetin, L.B. (Eds.), Foundations for Ecological Research West of the Antarctic
925 Peninsula, Antarctic Research Series 70. AGU, Washington, D.C., pp. 199-217.
926 Ross, R.M., Hofmann, E.E. and Quetin, L.B., editors, 1996b. Foundations for
927 ecological research west of the Antarctic Peninsula, Antarctic Research Series 70.
928 AGU, Washington, D.C., 448 pp.
929 Sherwin, T. J., 1988. Analysis of an internal tide observed on the Malin Shelf, north
930 of Ireland. Journal of Physical Oceanography 18, 1035-1050.
931 Sherwin, T.J. and Taylor, N.K., 1990. Numerical investigations of linear internal tide
932 generation in the Rockall Trough. Deep-Sea Research 37 (10), 1595-1618.
933 Simpson, J. H. and Rippeth, T., 1993. The Clyde Sea: a model of the seasonal cycle of
934 stratification and mixing. Estuarine Coastal Shelf Science 37, 129-144.
935 Small, L. F., Menzies, D.W., 1981. Patterns of primary productivity and biomass in a
936 coastal upwelling region. Deep Sea Research 28A, 123-149.

937 Smith, D. A. and Klinck, J.M., 2002. Water properties on the west Antarctic
938 Peninsula continental shelf: a model study of effects of surface fluxes and sea ice.
939 Deep-Sea Research II 49, 4863-4886.
940 Smith, D. A., Hofmann, E.E., Klinck, J.M., Lascara, C.M., 1999. Hydrography and
941 circulation of the West Antarctic Peninsula Continental Shelf. Deep-Sea Research I
942 46, 925-949.
943 Steele, M., Morison, J.H., Untersteiner, N., 1989. The partition of air-ice-ocean
944 momentum exchange as a function of ice concentration, floe size and draft. Journal of
945 Geophysical Research 94 (C9), 12739-12750.
946 Stigebrandt, A., 1976. Vertical diffusion driven by internal waves in a sill fjord.
947 Journal of Physical Oceanography 6, 486-495.
948 Stigebrandt, A., 1999. Baroclinic wave drag and barotropic to baroclinic energy
949 transfer at sills as evidence by tidal retardation, seiche damping and diapycnal mixing
950 in fjords. In: Muller, P., Henderson, D. (Eds.), Dynamics of Internal Gravity Waves
951 II, Proc. Aha Huliko' a Hawaiian Winter Workshop. University of Hawaii, Honolulu,
952 Hawaii, pp. 73-82.
953 Stigebrandt, A. and Aure, J., 1989. Vertical mixing in basin waters of fjords. Journal
954 of Physical Oceanography 19, 917-926.
955 Toole, J. M., 1981. Sea ice, winter convection and temperature minimum layer in the
956 Southern Ocean. Journal of Geophysical Research 86 (C9), 8037-8047.
957 Trenberth, K. E., 1984. Signal Versus Noise in the Southern Oscillation. Monthly
958 Weather Review 112 (2), 326-332.
959 Visbeck, M. and Fischer, J., 1995. Sea-Surface Conditions Remotely-Sensed by
960 Upward-Looking ADCPs. Journal of Atmospheric and Oceanic Technology 12 (1),
961 141-149.

Wallace, M.I., 2007. Ocean circulation, properties and variability in Marguerite Bay, west Antarctic Peninsula. PhD Thesis, The Open University, Milton Keynes, UK, unpublished.

Winant, C. D., 1980. Downwelling over the southern California shelf. Journal of Physical Oceanography 10, 791-799.

Woodworth, P. L., Vassie, J.M., Spencer, R. and Smith, D.E., 1996. Precise datum control for pressure tide gauges. Marine Geodesy 19, 1-20.

Woodworth, P.L., Hughes, C.W., Blackman, D.L., Stepanov, V., Holgate, S., Foden, P.R., Mack, S., Hargreaves, G.W., Meredith, M.P., Milinevsky, G. and Fierro Contreras, J.J., 2006. Antarctic Peninsula sea levels: a real time system for monitoring Drake Passage transport. Antarctic Science 18 (3), 429-436.

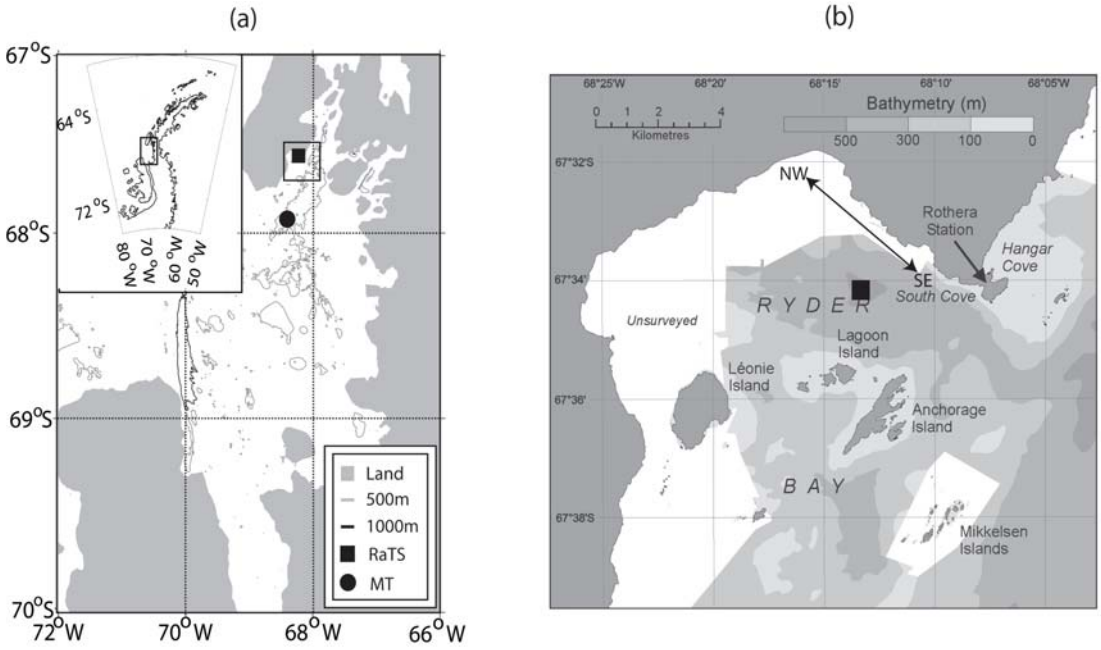

Figure 1: (a) Marguerite Bay (black box on inset of the Antarctic Peninsula). The coast, 1000m contour and 500m contours are delineated by thick grey, thin black and thin grey lines, respectively. The RaTS mooring (black square) and the MT mooring (black circle) are shown, and thick black lines delineate areas surrounding the moorings examined in Section 4.2. The area surrounding the RaTS mooring is expanded in (b), courtesy of the Mapping and Geographic Information Centre (MAGIC), BAS. The RaTS site is marked with a black square. The black, double-headed arrow shows the NW-SE wind orientation to which Section 4.1 refers.

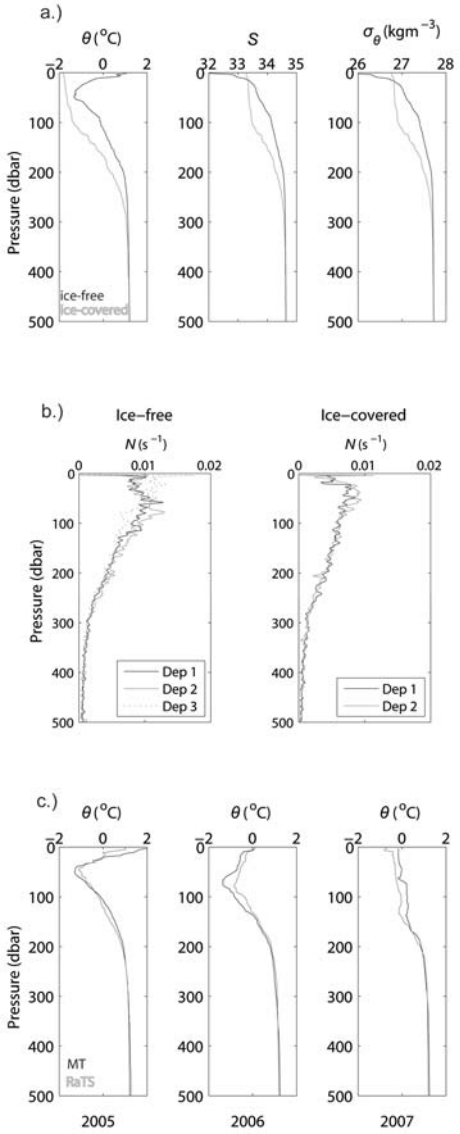

Figure 2: (a) Typical profiles of potential temperature, salinity and potential density anomaly from the RaTS site for the ice-free (black) and ice-covered (grey) seasons; (b) mean buoyancy frequency profiles for the ice-free and ice-covered seasons at the RaTS site (Dep 1, 2 and 3 refer to the deployment); and (c) comparison of potential temperature profiles from the RaTS site (grey) and MT (black) from January 2005, February 2006 and April 2007.

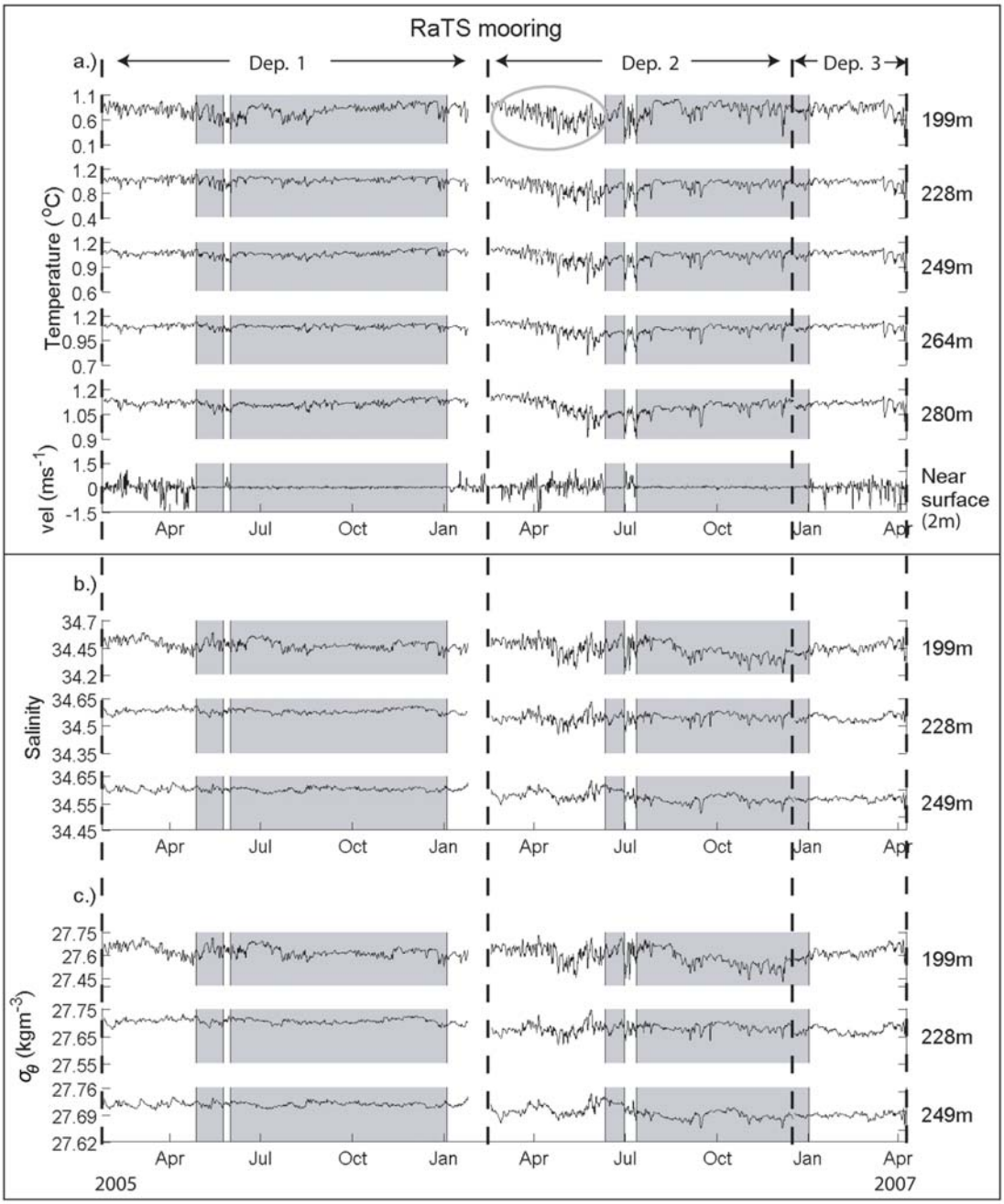

Figure 3: (a) Temperature, T, (b) salinity, S, and (c) potential density anomaly, σ_θ, time series from the RaTS site. Horizontal velocity data from the bin of the upward-looking ADCP closest to the surface are included at the bottom of panel (a). All time series are filtered using a 26-hour Butterworth lowpass filter to remove tidal and higher frequency variability. The velocity data are used to identify periods of ice cover (velocity variance is reduced in the presence of ice). Ice presence is shaded in grey on each panel. The three deployments are bordered by black dashed lines and the mean depth of each time series over the three deployments is noted to the right of each trace. The grey oval marks an example of the 2-7 day quasi-periodic signal examined in Section 4.1.

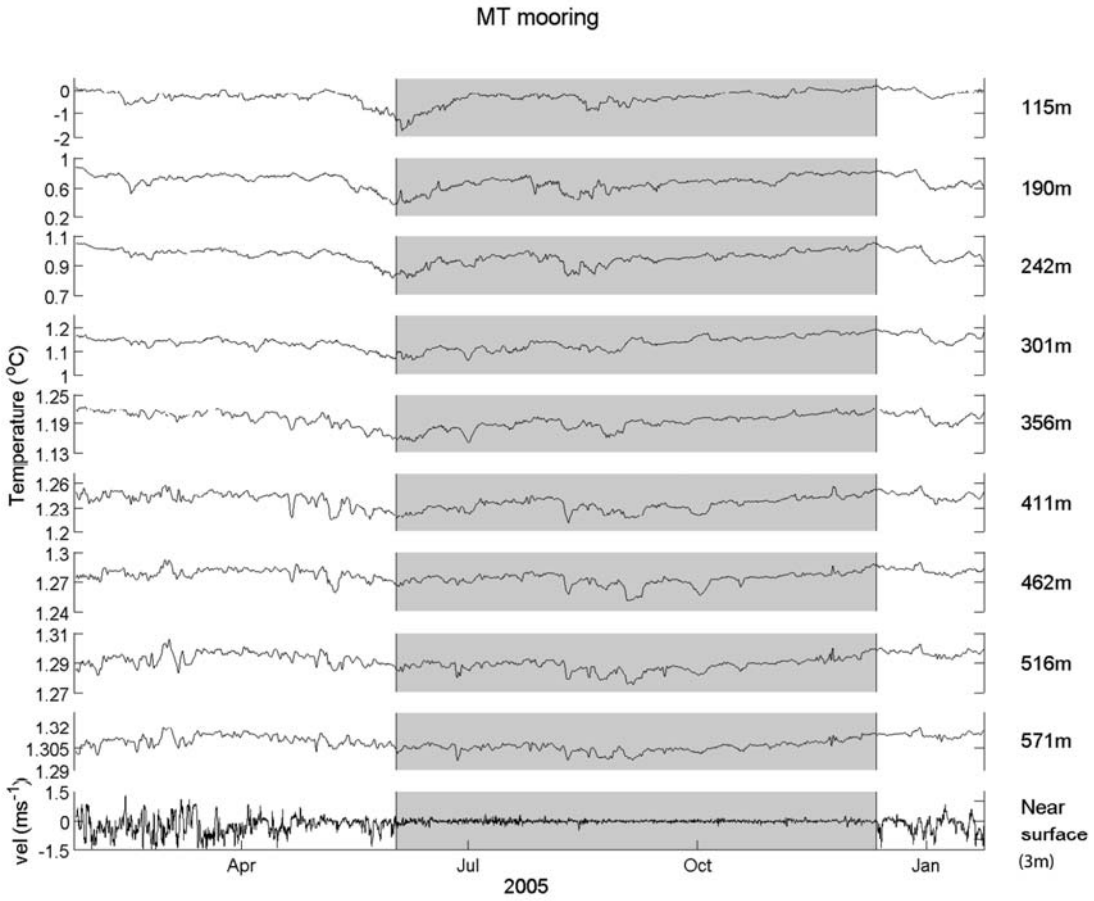

Figure 4: Temperature time series from the MT site. Horizontal velocity data from the bin of the upward-looking ADCP closest to the surface are included at the bottom of the panel. All time series are filtered using a 26-hour Butterworth lowpass filter to remove tidal and higher frequency variability. The velocity data are used to identify periods of ice cover (velocity variance is reduced in the presence of ice). Ice presence is shaded in grey on each panel. The depth of each time series is noted to the right of each trace.

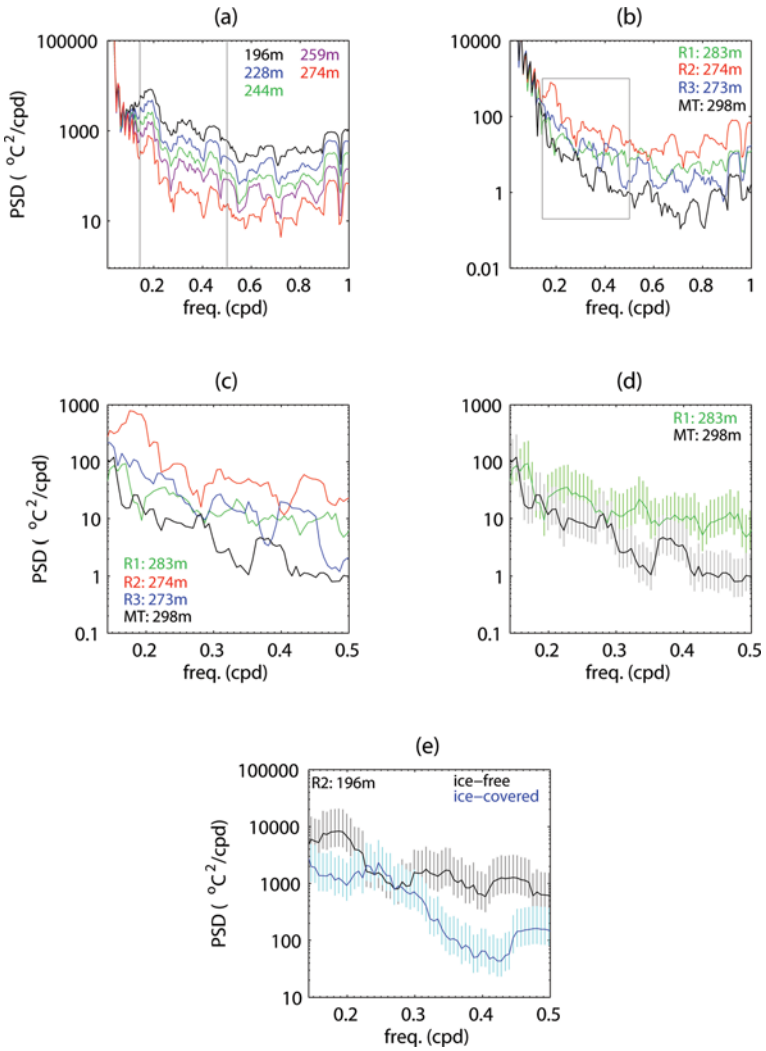

Figure 5: Log-linear plots of power spectral density (PSD) for 126-day temperature time series: (a) for all sensors from RaTS deployment 2 during the ice-free season; (b) 298m at MT, and 283m, 274m and 273m for RaTS deployments 1-3, respectively, for the ice-free season. The grey square marks the 2-7 day period, which is expanded in (c) for the four time series; (d) shows spectra from the MT mooring (black, 298m) and RaTS deployment 1 (green, 283m). Vertical lines represent the 95% confidence level; (d) shows spectra for the ice-free (black) and ice-covered (blue) seasons for RaTS deployment 2 (196m).

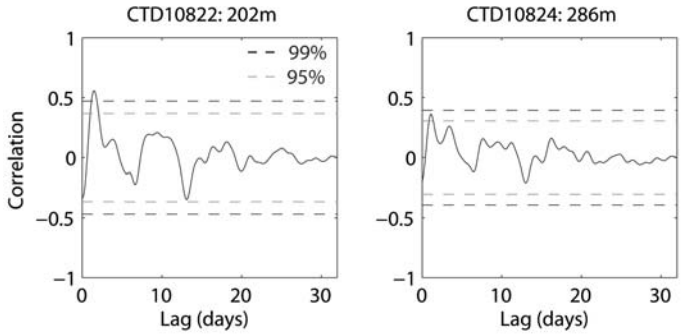

Figure 6: Correlations of temperature and NW-SE wind anomalies for the 30-day period 26/1/05-24/2/05 during the ice-free season of RaTS deployment 1. Both the wind and oceanographic data are filtered using a 26-hour Butterworth lowpass filter prior to correlation. The black and grey dashed lines represent the 95% and 99% significance levels, respectively.

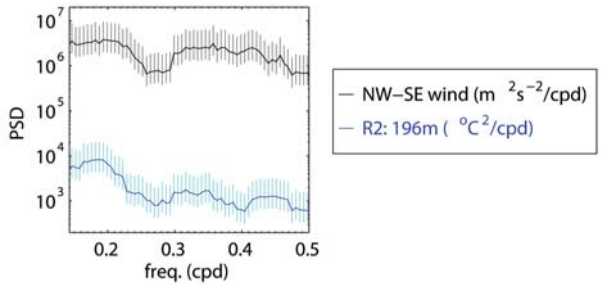

Figure 7: Log-linear plots of power spectral density (PSD) for the NW-SE wind (black) and temperature at 196m from RaTS deployment 2 during the ice-free season of 2006. Vertical lines represent the 95% confidence intervals for the wind (grey) and temperature (cyan) time series.

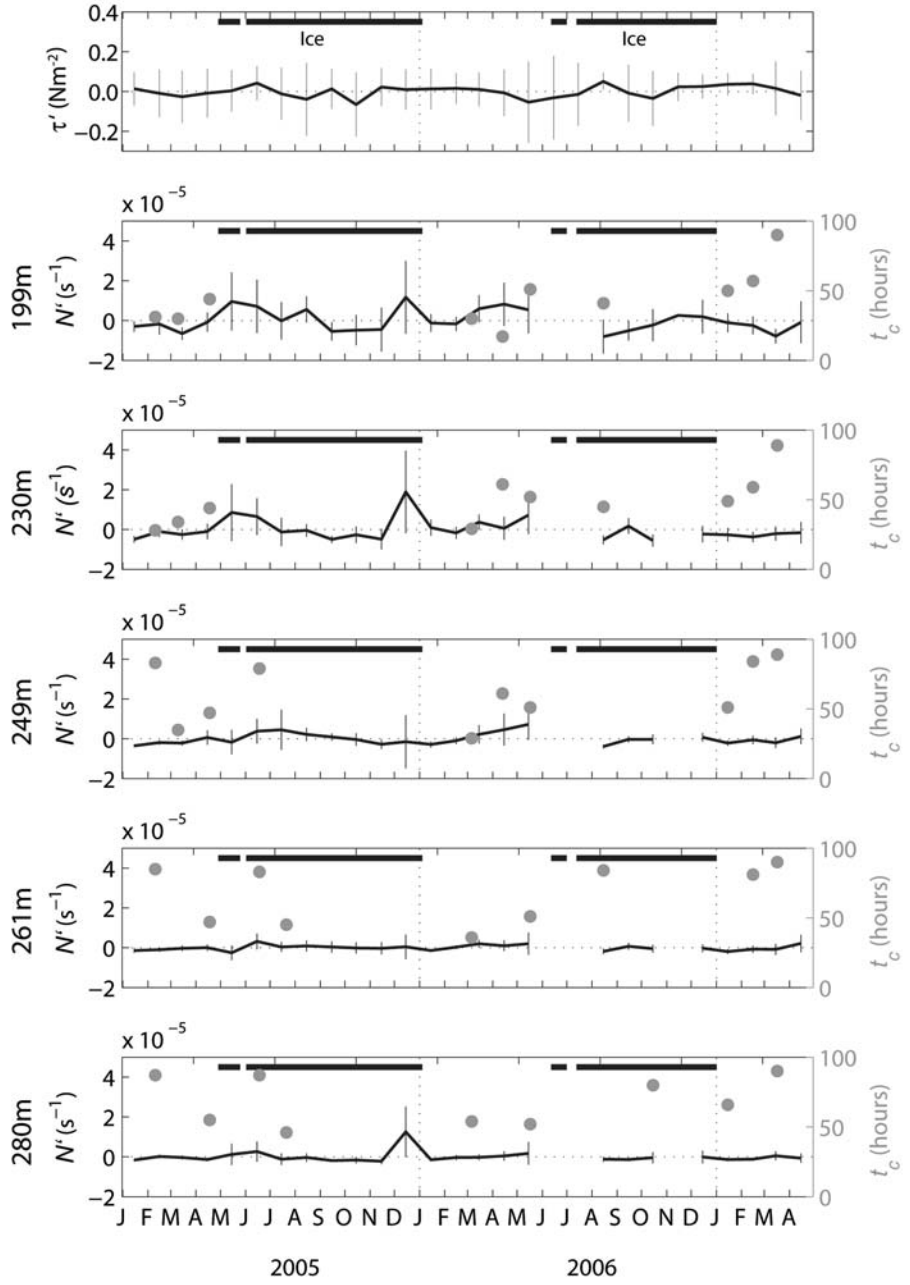

Figure 8: Time series of monthly mean NW-SE wind stress anomaly (τ') at Rothera station and monthly mean buoyancy frequency anomalies (*N*') from the RaTS CTD profiles for depths corresponding to those of the five temperature sensors on the RaTS mooring (missing data are due to gaps in the CTD sampling program). Vertical lines indicate ±1 standard deviation. The mean depth of each sensor over the three deployments is noted to the left of each plot. The timescales (t_c) at which temperature perturbations best correlate with cumulative wind stress are marked by the grey dots (only those correlations significant at the 95% or 99% level are included). The thick black lines indicate periods of sea ice cover.

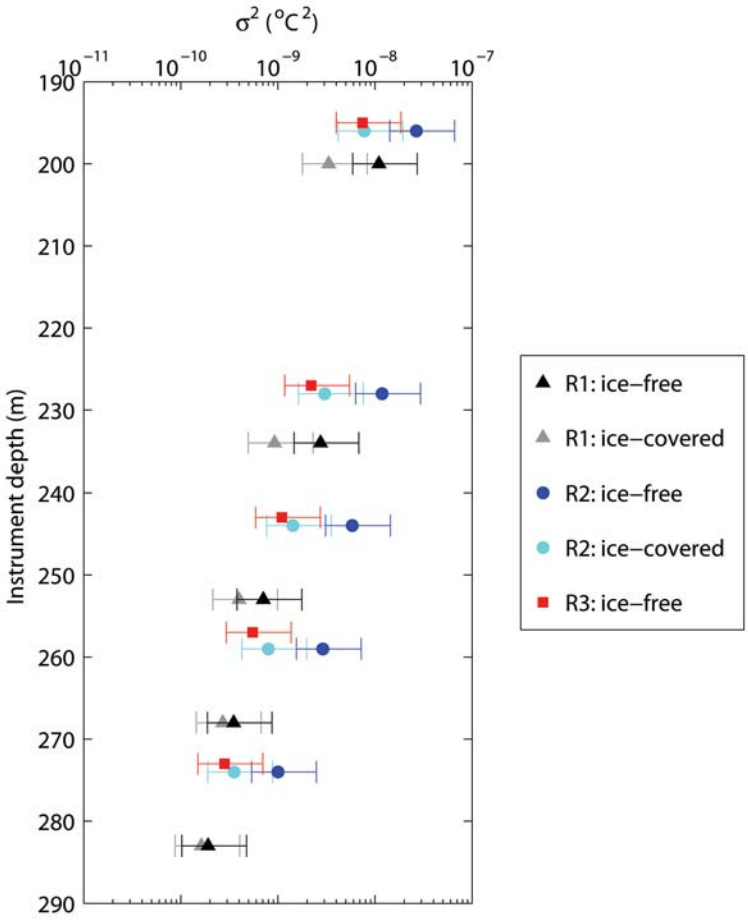

Figure 9: Log-linear plot of variance (σ^2) of temperature time series against instrument depth over the 2-7 day period for the ice-free and ice-covered seasons of the three RaTS deployments. Deployment 1 is represented by triangles (black and grey for the ice-free and ice-covered seasons, respectively); deployment 2 by circles (dark and light blue); and deployment 3 by red squares. Bars represent 95% confidence intervals.

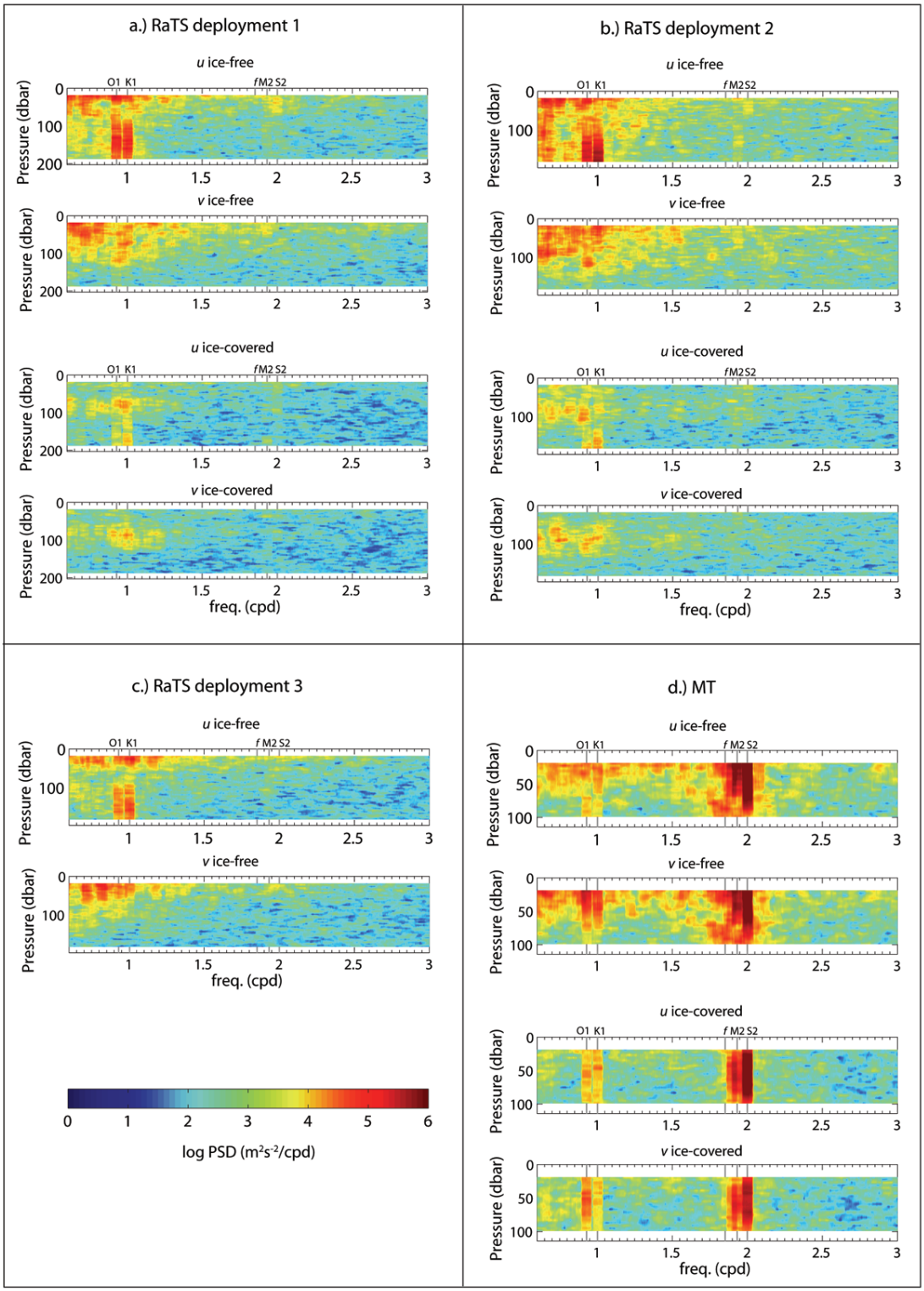

Figure 10: Contour plots of power spectral density (PSD) for east (*u*) and north (*v*) velocities from the moored ADCPs at (a-c) the RaTS site for all deployments and (d) MT. Spectra for both the ice-free and ice-covered seasons are included, where available. The O1, K2, M2, S2 and inertial (*f*) periods are marked. Note the different depth scales at the two mooring sites. Frequency measured in cycles per day.

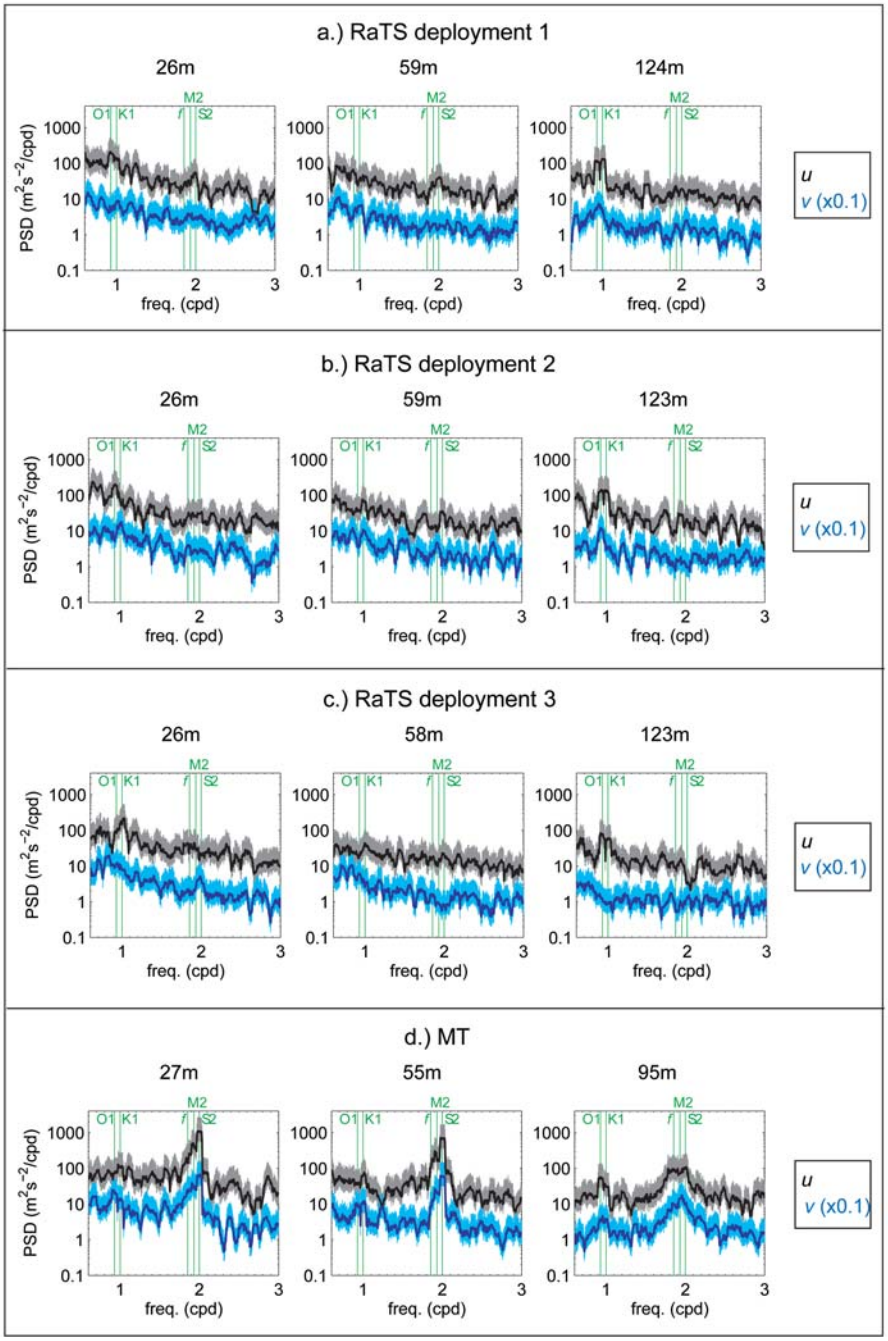

Figure 11: Confidence levels for ADCP velocity PSD for selected depths from (a-c) the three RaTS deployments and (d) MT. Eastward velocity (u) and northward velocity (v) are shown in black and dark blue, with their respective 95% confidence levels in grey and light blue. PSD(v) is multiplied by 0.1 for ease of viewing. Frequencies of the O1, K1, M2 and S2 semidiurnal tides are marked in light green, as is the inertial frequency, f.

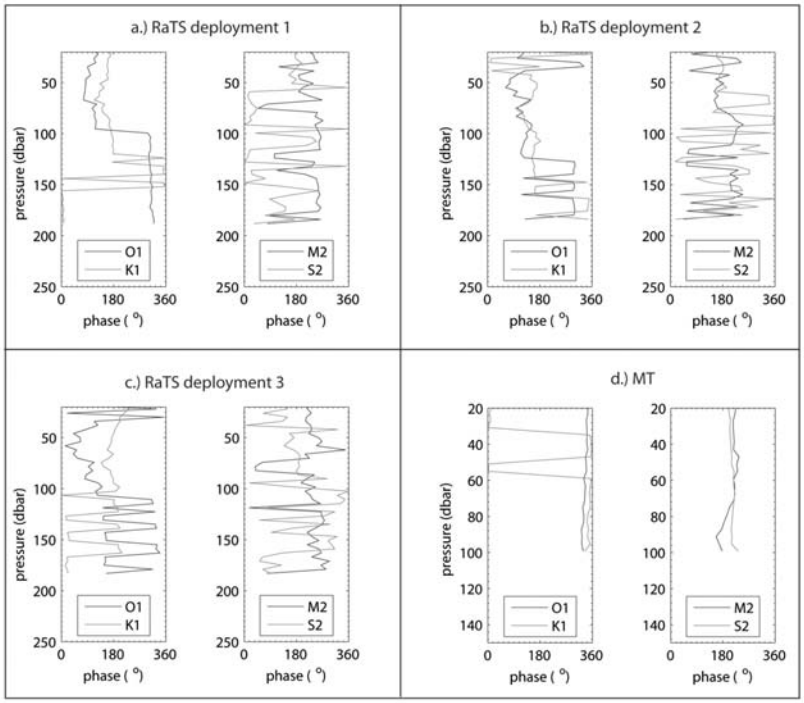

Figure 12: Profiles of tidal phase for the diurnal O1 and K1, and semidiurnal M2 and S2 tides for the three RaTS deployments and MT. Profiles are extracted from the ADCP data using the harmonic analysis package, T_TIDE (Pawlowicz et al., 2002).

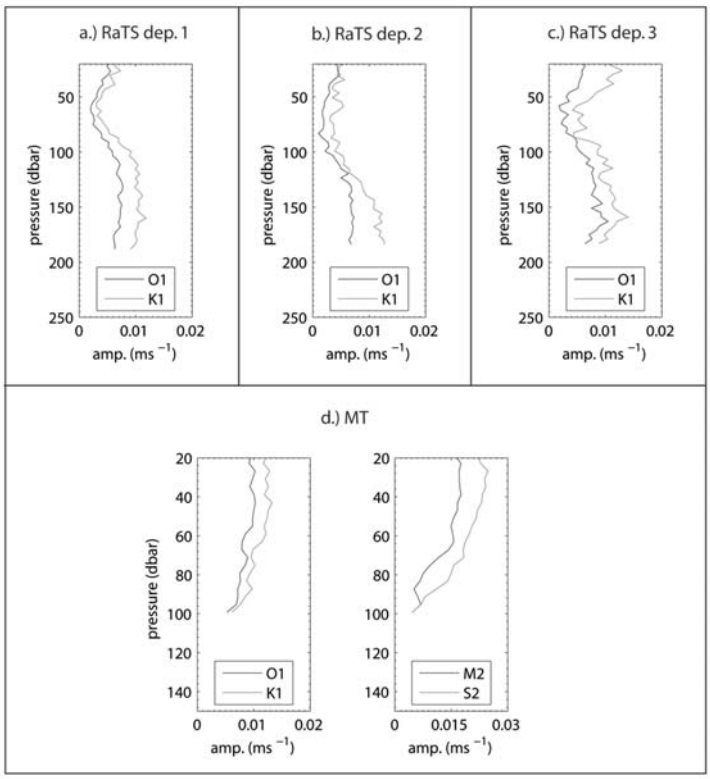

Figure 13: Profiles of tidal amplitude for the diurnal O1 and K1 tides for the (a-c) three RaTS deployments and (d) MT, and the semidiurnal M2 and S2 for MT. Profiles are extracted from the ADCP data using the harmonic analysis package, T_TIDE (Pawlowicz et al., 2002).

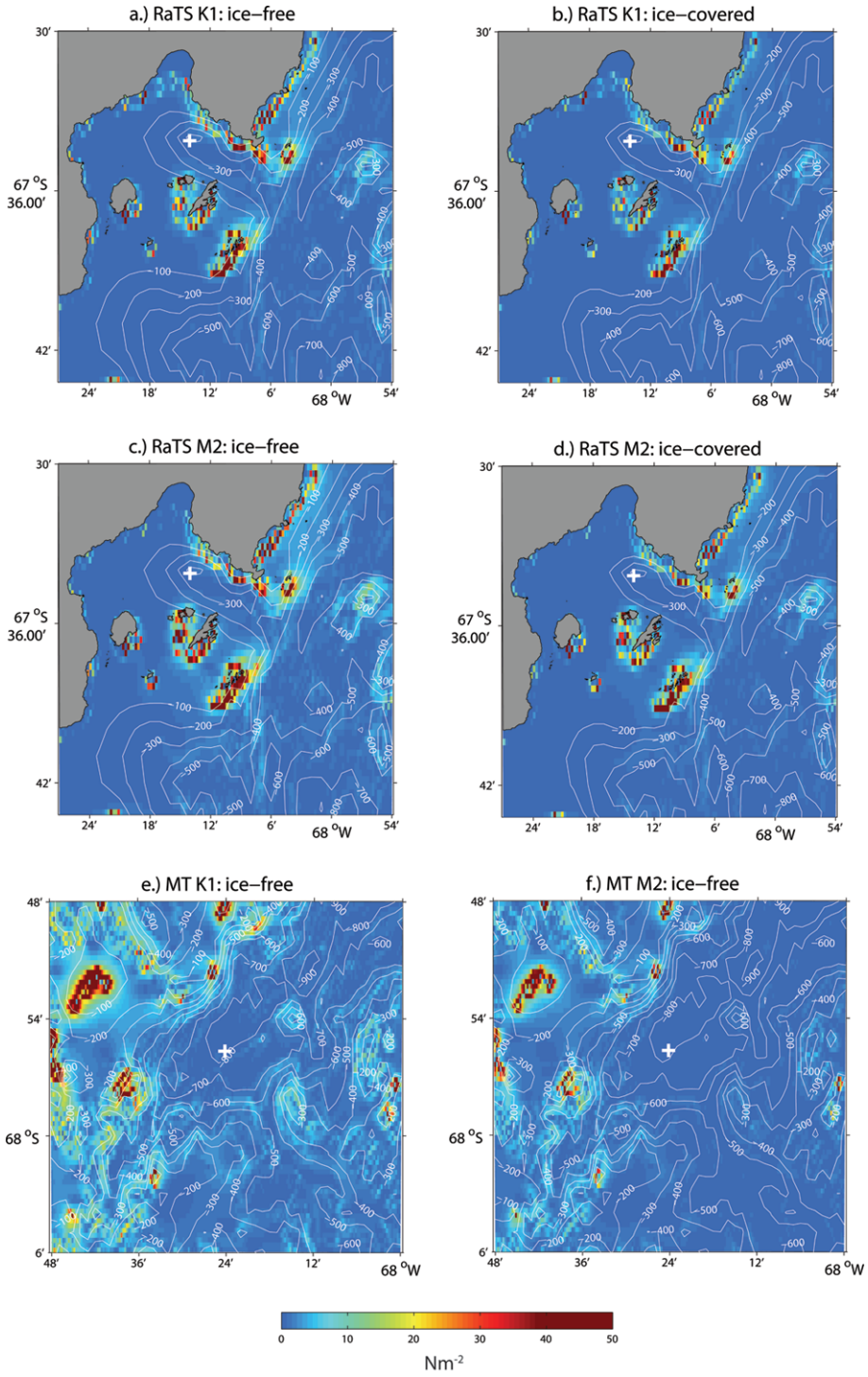

Figure 14: Depth integrated tidal forcing function (F^*) calculated for (a, b) the K1 and (c, d) the M2 tides during the ice-free and ice-covered seasons of RaTS deployment 1, and (e, f) the K1 and M2 tides during the ice-free season at MT. The mooring locations are signified by white crosses and contoured depths are in metres (courtesy of the SO-GLOBEC program). The land is shaded grey and detailed coastline data for Ryder Bay are courtesy of MAGIC, BAS.

Mooring	Water depth (m)	Deploy-ment	Location (deg, min)	Deployed	Recovered	Deployment length (days)
RaTS	520	1	67° 34.02'S 68° 14.02'W	25/01/05	15/02/06	387
		2	67° 33.97'S 68° 14.06'W	17/02/06	16/12/06	303
		3	67° 34.01'S 68° 14.00'W	17/12/06	09/04/07	114
MT	840	1	67° 55.39'S 68° 24.15'W	24/01/05	15/02/06	388

Table 1: Deployment details for the Marguerite Bay moorings

Instrument	Sampling period	Deployment	Depth (m) [Pressure (dbar)]
RaTS site			
CTD & 75kHz ADCP	CTD: 1 hour ADCP: 15 min. ensembles	1	200 [202]
		2	196 [199]
		3	195 [197]
TR	1 hour	1	~234
		2	~228
		3	~227
CTD	1 hour	1	253 [255]
		2	244 [246]
		3	243 [245]
TDR	1 hour	1	268 [271]
		2	259 [261]
		3	257 [260]
CTD	1 hour	1	283 [286]
		2	274 [277]
		3	273 [276]
MT site			
CTD & 75kHz ADCP	CTD: 1 hour ADCP: 15 min. ensembles	1	114 [115]
TR	1 hour	1	~185
TDR	1 hour	1	240 [242]
CTD	1 hour	1	298 [302]
TR	1 hour	1	~352
TDR	1 hour	1	406 [411]
CTD	1 hour	1	457 [462]
TR	1 hour	1	~511
TDR	1 hour	1	564 [571]

Table 2: Mooring configurations. Abbreviations are as follows: CTD = conductivity-temperature-depth sensor; TDR = temperature-depth recorder; TR = temperature recorder; ADCP = Acoustic Doppler Current Profiler. Depths of some instruments are approximate in the absence of pressure data.

Deployment	Season	Dates
1	Ice-free	26/01/05-24/02/05 27/02/05-28/03/05 03/04/05-02/05/05
1	Ice-covered	03/06/05-02/07/05 06/07/05-04/08/05 15/09/05-14/10/05
2	Ice-free	18/02/06-19/03/06 28/03/06-26/04/06 30/04/06-29/05/06
2	Ice-covered	30/07/06-28/08/06 31/08/06-29/09/06 30/09/06-29/10/06
3	Ice-free	31/12/06-29/01/07 30/01/07-28/02/07 02/03/07-31/03/07

Table 3: Time periods over which correlations were carried out between winds at Rothera and moored temperature time series.

Deployment	Depth (m)	$\frac{\sigma^2_{no\ ice}}{\sigma^2_{ice}}$	$\frac{\sigma^2_{no\ ice}[2]}{\sigma^2_{no\ ice}[1,3]}$	$\frac{\sigma^2_{ice}[2]}{\sigma^2_{ice}[1,3]}$
1	200	3.29	2.41	2.33
	~234	2.97	4.31	3.29
	253	1.78	8.16	3.58
	268	1.30	8.28	2.94
	283	1.17	5.23	2.17
2	196	3.40		
	~288	3.89		
	244	4.06		
	259	3.65		
	274	2.83		
3	195		3.56	
	~227		5.38	
	243		5.26	
	257		5.27	
	273		3.56	

Table 4: Comparison of variance over the 2-7 day period from the ice-free and ice-covered seasons for all instruments from the three RaTS deployments. Comparisons include variance during the ice-free season divided by variance during the ice-covered season; variance during the ice-free season of deployment 2 divided by the corresponding data from the other two deployments; and variance from the ice-covered season of deployment 2 divided by that from the ice-covered season of deployment 1.

Tidal con.	Freq. (cpd)	RaTS site		MT site	
		u amp. (cms^{-1}) [phase (°)]	*v* amp. (cms^{-1}) [phase (°)]	*u* amp. (cms^{-1}) [phase (°)]	*v* amp. (cms^{-1}) [phase (°)]
M2	1.9323	1.05 [40.32]	3.24 [186.88]	0.37 [179.53]	0.17 [321.23]
S2	2.0000	1.68 [141.95]	2.54 [254.65]	0.59 [320.86]	0.57 [193.59]
K1	1.0027	0.83 [169.57]	0.39 [294.51]	0.39 [335.22]	0.36 [211.57]
O1	0.9295	0.78 [149.15]	0.97 [273.21]	0.34 [324.49]	0.23 [205.07]

Table 5: Amplitude and phase of the eastward (*u*) and northward (*v*) components of the dominant diurnal and semidiurnal tides for the two mooring sites. Data are from the AntPen04.01 tidal model (Padman, unpublished; www.esr.org/ptm_index).